The Thesis Committee for Ifedioranma Anyaegbunam
Certifies that this is the approved version of the following thesis:

The Development of a Battery Management System with Special Focus on Capacity Estimation and Thermal Management

APPROVED BY
SUPERVISING COMMITTEE:

Supervisor:

Dongmei Chen

Joseph Beaman

The Development of a Battery Management System with Special Focus on Capacity Estimation and Thermal Management

by

Ifedioranma Anyaegbunam, B.S.M.E.

Thesis

Presented to the Faculty of the Graduate School of

The University of Texas at Austin

in Partial Fulfillment

of the Requirements

for the Degree of

Master of Science in Engineering

The University of Texas at Austin

August 2016

Dedication

To my mother and father for their love, patience and fierce support and my close friends for their understanding.

Acknowledgements

First of all, I would like to thank my parents who have stood by me and pushed me further than I thought I could go.

Secondly, I want to thank my advisor Dr. Dongmei Chen who has supported me intellectually and financially and who has become one of the best mentors I have ever had the pleasure of working with. Next, I would like to thank Dr. Joseph Beaman for being the second reader on my thesis and providing insightful and useful feedback.

I also want to thank all of my lab mates in Dr. Chen's lab for their support and ideas. I especially want to thank Dr. Victor Yu and Dr. Alex Headley. I thank Dr. Yu for providing guidance on multiple occasions with regard to research direction, scope and methodology. I also thank Dr. Headley for his support in figuring out how to model the thermos-fluid asked of the battery thermal management system simulation for his help with troubleshooting the nonlinear Kalman Filters. Etse Campell also deserves thanks for her collaboration on the thermal management portion of my research.

Finally, I want to thank all of my friends, both old and new, for their tireless support, empathy and patience as well as the NSF for their financial support.

Abstract

The Development of a Battery Management System with Special Focus on Capacity Estimation and Thermal Management

Ifedioranma Anyaegbunam, M.S.E.
The University of Texas at Austin, 2016

Supervisor: Dongmei Chen

Lithium ion batteries are instrumental in tackling the challenges of global warming. They have shown great utility in electric and hybrid vehicles. However, challenges with regard to performance and safety such as capacity fade and thermal runaway need to be accounted for in the implementation of these battery systems. One way is through battery management systems that monitor and control various aspects of the battery's operation. At the heart of the battery management system is an analytical model of the battery. This thesis proposes a battery management system which uses a "low-order" physics-based battery model that estimates capacity and optimally manages the temperature of the battery.

A capacity estimation methodology is proposed that uses the state of charge estimate from an Extended Kalman filter and the inverse of the coulomb counting equation to estimates the "instant" capacity of the battery. This instant value is then used in an averaging calculation that uses saturation limits and a time delay to obtain a value

for the capacity that is representative of the battery. This value is then feedback into the kalman filter. The capacity estimate obtained through this method was between 2 and 8 % off of the true value.

A thermal management system is also proposed that optimally controls a fan to cool a lithium ion battery. The system was developed and tested in a simulated environment. First, the fan model was integrated with the battery model and simulations were run to test the open loop temperature response of the battery to the fan cooling while varying the input voltage of the fan the current demanded of the battery. From this data an operating point was chosen, the system was linearized, and a linear quadratic controller was designed and implemented. The controller was sluggish when faced with a temperature perturbation in the absence of a current demand increase but drove the temperature change to zero. In the presence of a current change, the controller drove the state to a nonzero steady state value. The same result occurred when a disturbance rejection mechanism was applied to the controller.

Table of Contents

List of Tables

List of Figures

Chapter 1: Introduction

1.1 BACKGROUND

Global warming is one of the defining issues of our time and the greenhouse gasses released into the atmosphere as a result of the world's transportation trends and habits is a large part of the problem. Between the years of 1990 and 2014, Americans enjoyed a long period of economic growth which allowed them to start families and move farther out of the city center and into the suburbs [1]. The effect of all these factors was a 37% increase in miles driven over this period [1].These trends plus increases in commercial transportation lead to a 17% increase in the proportion of greenhouse gases released into the atmosphere by transportation between 1990 and 2014 [1]. This is despite advances in fuel efficiency [1] and electric and hybrid vehicles. In fact, in 2014 over a quarter of the total greenhouse gasses released into the atmosphere by Americans were the result of personal and commercial transportation [1].

Such trends are not unique to the United States either. For example in India, vehicle sales have increased at an alarming rate (around 60% between 2007 and 2012) [2]. This is most likely due to the fact that India is one of the fastest growing economies in the world [3]. Furthermore, it is estimated that India could have upwards of 250 million vehicles on the road by 2025 [2]. With all these cars and motorbikes entering the market it is only logical that the environmental impact would be substantial. In fact, the impact of all the vehicles already on the road has been deadly for some Indians [2]. Particulate matter pollution is especially troublesome as one third of it comes from the

transportation sector and is the 6th leading cause of death among Indian residents due to diseases caused by the pollution [2]. With all these issues related to pollution, it is especially troubling that India's light duty vehicle fleet does not currently adhere to any CO2 emissions standards or efficiency standards [2].

India is not the only country struggling to find a balance between the demands of a growing economy and the environmental impact of said growth. China is currently grappling with similar concerns as its economy grows and an increasing number of its citizenry enter the middle class. A side effect of this growth has been that between the years of 2000 and 2010 CO2 emissions from the transportation sector have doubled [4]. While it should be noted that transportation makes up a relatively small percentage of China's total carbon emissions [5]; there is still concern and action on the part of the Chinese government to reduce these emissions [4]. Proof of said concern is the fact that the Chinese government set a goal to reduce carbon intensity throughout its economy by 2020 [4]. However, according to the ICCT, in order to accomplish this task they will need to reduce transportation sector carbon emission growth by about 50% [4].

The challenges in reducing carbon emissions are immense and the solutions to these challenges will have to be multifaceted. One such solution is through engineering and technology, specifically Lithium-ion battery technology. Lithium ion batteries have become the dominate battery type in both electric and hybrid vehicles due to decades of innovation and research and have the potential to reduce a large percentage of emissions from the transportation sector. In fact, when factoring in the emissions generated at

power plants due to the charging of EVs, PHEVs and HVs, current electric and hybrid vehicles still offer roughly a 50% reduction in CO2 emissions when compared to pure gasoline powered vehicles [6].

1.2 LITHIUM ION BATTERY MECHANISMS AND HISTORY

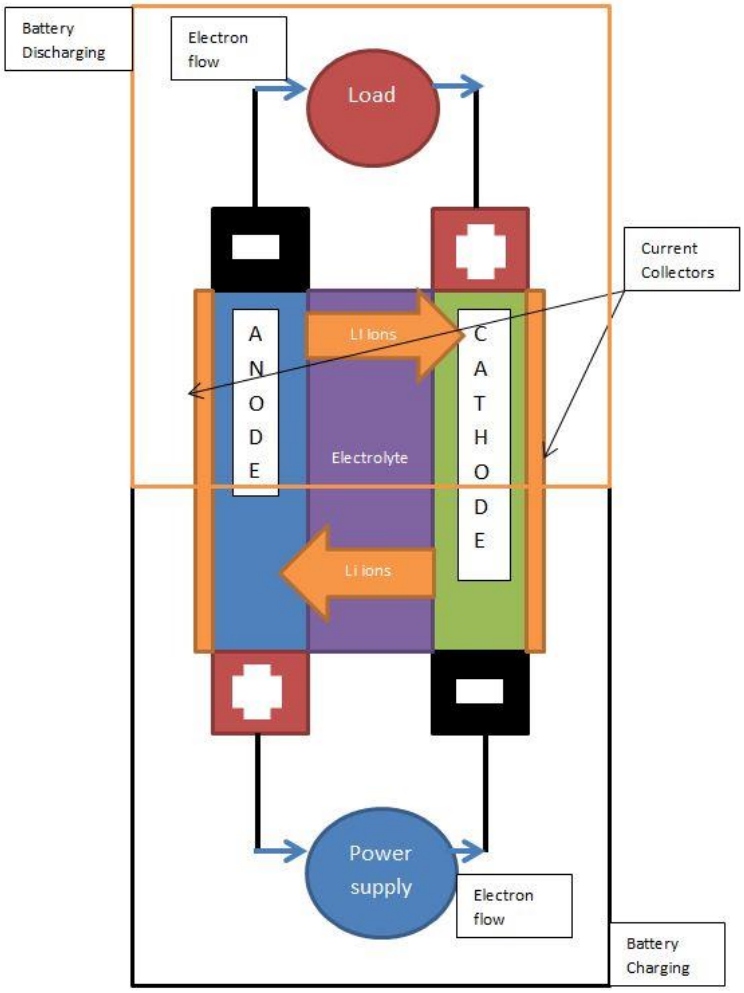

Figure 1.1: Diagram of battery charge and discharge [7]

Figure 1.1 shows a schematic of a basic lithium ion battery. A Lithium ion battery is comprised of a few basic components. During the charging process of a Lithium ion

battery the anode donates electrons, the cathode accepts electrons, the electrolyte facilitates the flow of ions between the cathode and anode, and the current collectors facilitate the flow of electrons between the cathode and anode. The historical development of the rechargeable lithium battery is a history of intense exploration that birthed a marvelous innovation. The sections below will provide more details on the development of the anode, cathode and electrolyte.

1.2.1 Anode Development

Modern day lithium ion batteries have graphite anodes that allow for the intercalation of lithium ions into their material matrix [8]. The reason for the use of graphite can be found the historical development of the anode. The original Lithium based batteries were developed in the early 1900s and used Lithium metal as their anodes [8]. These were "primary" batteries meaning that they were not rechargeable [8]. When study into rechargeable lithium based batteries started in the 70s [9], the scientists ran into serious problems when cycling the cells such as shorting and thermal instability [8]. These issues were caused by dendrites that develop from the lithium anode and grow due to cycling until they make contact with the cathode and short the cell [8], [9]. Since Lithium metal could no longer be used as an anode focus shifted to cathode development [8].

1.2.2 Cathode Development

Cathodes in most contemporary lithium ion batteries are Lithium metal oxides due to the large voltage differential they provide relative to ionic lithium [9]. This is an important feature of the cathode because it is a large factor in how much energy the battery cell possesses [9]. This development can be traced back to the work of Dr. John B. Goodenough who in the 80s developed the Lithium-cobalt-oxide battery as a solution to the dendrite formation problem encountered with lithium anodes [8]. These types of cathodes have various crystalline structures that contain pockets of space called "holes" that allow for the intercalation of lithium ions [9].

1.2.3 Electrolyte Development

In most contemporary cells the electrolyte is a type of organic solvent polymer that possesses large voltage "windows" thus allowing for higher energy cells [9]. Aqueous electrolytes were tried first but they were abandoned for many commercial cells due to their small voltage "window" which limits how energetic a cell can be and determines the stability of the electrolyte [9].

1.3 Discussion of Different Lithium Ion battery types

There are numerous different chemistries for lithium ion battery cells each with strengths and weaknesses which affect their application. These different categories are typically denoted by the chemistry of their cathodes and are discussed below.

1.3.1 Lithium Cobalt Oxide

The Lithium Cobalt Oxide battery was the chemistry pioneered by Dr. Goodenough in the 1980s and which gained popularity in the 90s through the efforts of Sony [8]. This battery chemistry has a high capacity relative to its weight (140 mAh/g) [10] which is due in part to the high potential that Lithium cobalt oxide has relative to ionic lithium [9]. However, this particular chemistry possesses numerous drawbacks including poor thermal characteristics, low cycle life when compared to other chemistries, and the ability to be safely cycled at aggressive C-rates relative to its own C rating [11]. These three issues are caused by the fact that high C rates in turn cause a high rate of lithium removal from the cathode which can lead to oxygen evolution [10]. To make matters worse, according to Bang et al (cited in [10]), this oxygen evolution can then undergo combustion with the organic electrolyte and heat up the cell [10]. It is evident based on these drawbacks that such a battery would be a poor choice for electric vehicles due to the variable environments in which these vehicles operate [9].

1.3.2 Lithium Nickel Manganese Cobalt Oxide

Lithium Nickel Manganese Cobalt oxide chemistry addresses many of the issues present in Lithium Cobalt Oxide. This chemistry has a much higher specific capacity than Lithium Cobalt oxide (140 mAh/g for LiCoO2 vs 200 mAh/g for LiNixMnyCozO2) [10]. The inclusion of Nickel and Manganese allow for a very flexible chemistry architecture enabling its use in a host of applications [11]. This flexibility is made possible by the

numerous ratio combinations that the main components (Nickel, Manganese and cobalt) can be mixed in [11]. Due to this combination of elements, this battery chemistry is fairly balanced in terms of performance in extreme temperatures, specific energy, power and cost [11]. The one major drawback for this particular chemistry is that it is prone to a phenomenon called “cation mixing” [10] where the Ni ions can fill up sites meant for the Li ions thus negatively impacting its performance [12].

1.3.3 Lithium Nickel Cobalt Aluminum Oxide

This chemistry is similar to Lithium Nickel Manganese Cobalt Oxide but is more expensive [11]. However, it has a higher specific energy which makes it an attractive option or electric vehicles and electric vehicle companies such as tesla [11]. Another reason such a battery may be attractive for EV applications is that it is capable of fast charging [11] which is essential to the growth of electric vehicles in the marketplace.

1.3.4 Lithium Iron Phosphate

Lithium Iron Phosphate batteries are very robust when compared to other battery chemistries in their response to extreme charging conditions [11]. This chemistry is also devoid of the toxicology issues that plague the cobalt based chemistries [10]. However, this particular chemistry has a low capacity relative to the others [11].

1.4 BATTERY MANAGEMENT SYSTEMS

Despite major advances in Lithium ion battery technology, there are still issues that plague this particular type of battery across the different chemistries that require careful monitoring and regulation of the pack itself. This monitoring and regulation is done by a battery management system (BMS) which is a computer system that uses an analytical model of the battery, sensors and actuators to monitor and control variables such as temperature, state of charge, and voltage. In order to do its job adequately the BMS needs accurate sensors and a detailed model of the battery. Two of the major issues with battery management systems have been capacity estimation/ capacity fade prediction and thermal regulation. The capacity estimation is important for accurate state of charge estimation [13] and for tracking of battery state of health and the thermal regulation is important in order to prevent thermal runaway. Numerous scientists have pursued work trying to solve both of these problems their work is reviewed in the next chapter.

Chapter 2: State of the Art for Battery Management Systems

2.1 Capacity Estimation and Capacity fade Prediction State of the Art

Capacity fade is a term that describes the reduction of the amount of charge the battery can hold relative to the date of its manufacture. Various chemical processes that occur within the cell that are greatly affected by both the performance demands placed on the cell and the environment in which the cell functions cause capacity fade [14]. More specifically, capacity fade is caused by various mechanisms which reduce the amount of transportable lithium ions in the cell [14]. The majority of these mechanisms occurs at the negative electrode and includes the formation and growth of the solid electrolyte interphase layer, further degradation of the electrode through interaction with the solvent, and lithium plating of the electrode due to low diffusion rates in cold weather [14]. These are complex processes that are difficult to model fully [14] and many are not feasible to include in control oriented models of lithium ion batteries. Therefore, many researchers have focused on other ways to observe and predict the capacity fading phenomena of lithium ion batteries. The two major methodologies used to this end are ones that require large datasets for learning like neural networks and ones that only require real time data input like extended Kalman filters. Both types are discussed in the sections below.

2.1.1 Learning based Methodologies

Eddahech et al leveraged large data sets in order to both create a simple equivalent circuit model of a high powered lithium ion battery and to create a recurrent neural network to perform step-ahead prediction of capacity fade and internal resistance growth [15]. Chrono-potentiometry and electrochemical impedance spectroscopy tests results were used to generate the equivalent circuit model [15]. The recurrent neural network was trained using data from various power cycle tests and provided very accurate prediction results when compared to the actual capacity fade profile of the battery [15]. Data driven methodologies like the one described are powerful because they can be applied to almost any system so long as enough data exists. However, collecting such data is time consuming and costly.

A related concept to neural networks are support vector machines. Pattipati et al developed a method which involved the use of an equivalent circuit model of a lithium ion battery and support vector machines to estimate and predict state of charge and capacity fade of the battery [16]. This paper also proposed the use of a hidden markov model to calculate a "survival function" which calculates the likelihood of a battery failing in the future from information available at the current time step [16]. Both of these methods were used to great effect in the estimation and prediction of capacity fade and remaining useful life. However, they admitted to not including the aging phenomena of other parameters in the battery [16] which could contribute to capacity fade [14].

Wei et al developed a simple, data driven model of lithium ion battery capacity fade which did not explicitly include any dependence on environmental impacts on the battery (ex. Temperature) [17]. This model then has its parameters initialized using Dempster-shafer theory and extensive capacity fade data [17]. Once the initialization is complete a Bayesian Monte Carlo scheme, which is a model based methodology, is employed to do step-ahead prediction and calculate remaining useful life [17]. They proved that this methodology was superior to extended Kalman filtering for multistep ahead prediction [17]. This methodology is similar to the work completed by Bai et al, which involved using both a feedforward neural network (data based methodology) and a duel extended Kalman filter to estimate capacity [18]. Data driven models have shown to be powerful and effective at estimating and predicting capacity fade. However, such methods require vast sums of data and run the risk of overfitting [19] which can restrict the use an already developed model to a small subset of batteries. The use of model based approaches like nonlinear Kalman filters eliminate the need for large storage of data and can be effectively combined with data driven methods to obtain a powerful effect.

2.1.2 Model based Methodologies

Hu et al developed a multiscale framework for estimating state of charge and capacity [13]. It works by using a modified Dual extended Kalman filter in which one Kalman filter uses the voltage to estimate the state of charge and the other uses the state of charge to estimate the capacity with the SOC extended Kalman filter running at a much faster rate than the capacity extended Kalman filter [13]. The paper proved that this

scheme was much faster and more accurate than the typical dual extended kalman filtering method [13]. However, there would be periods where the accuracy of the estimate degrades but it always restores itself eventually [13].

A similar methodology was developed by Kim where he used a simple equivalent circuit model of a lithium ion battery and a dual sliding mode observer, both operating at different time-scales. They use lyapanov functions as their basis to estimate both state of charge and capacity fade [20]. This methodology has the benefits of being less complex mathematically than kalman filtering while producing low error estimates of state of charge and capacity [20].

Qiuting et al developed a methodology of estimation state of charge and state of health using dual unscented kalman filtering in conjunction with a two-order equivalent circuit model of a lithium ion battery [21]. This methodology differs from the other two in that they use internal resistance as their measure of state of health instead of capacity fading [21]. They developed the methodology and then ran both simulation tests and physical tests to validate their estimation scheme [21]. Their method seems to track state of charge and state of health somewhat adequately but not as well as some of the other methods discussed within this review.

These methodologies have been shown to be fairly effective at estimating capacity and predicting capacity fade. However, they all use some form of equivalent circuit model which does not fully describe the electrochemical processes of the battery. The use of an accurate, physics based battery model could improve the accuracy of these methodologies.

2.2 THERMAL MANAGEMENT STATE OF THE ART

The large body of work related to the thermal management of lithium ion batteries can be divided into two main categories: passive cooling and active cooling. Passive cooling methodologies are those that do not use external power sources to cool the battery pack. On the other hand, active cooling methodologies do use external energy to power fans, pumps or other actuators used to cool lithium ion batteries.

2.2.1 Passive Cooling Methodologies

In studies concerning passive cooling methodologies, variations of one type of system seem to dominate: systems using Phase change materials. Phase change materials are materials that absorb heat by transforming from one state of matter to another [22]. Khateeb et al utilized PCMs to great effect when they designed and simulated a PCM based thermal management system for a lithium ion battery powered scooter [23]. However, they also found that in extreme ambient temperatures the PCM alone was not powerful enough to thermally protect the battery from damage so they added other cooling methods to compensate for the weakness [23]. It must also be mentioned that while the work done by Khateeb et al is valuable, the study was on a vehicle much smaller than the electric cars such systems might eventually be used. These larger systems will no doubt experience similar phenomenon to what was observed in Khateeb et al's work but at a much greater intensity.

One group of researchers who addressed this concern was Li et al who designed and tested a phase change material and metal foam hybrid system in order to passively

manage the thermal properties of a high powered lithium ion battery that might be used in a full size electric vehicle [24]. They found the methodology to be highly effective at regulating temperature especially when the foam used had a low porosity [24].

Sabbah et al compared a purely active air cooling scheme to a pure PCM cooling scheme in order to determine which was superior [22]. The researchers tested the schemes both through simulation and physical testing and found the PCM scheme to be superior in terms of regulating both temperature and temperature variance throughout the battery pack [22].

It is clear that PCM systems are very capable at temperature regulation; however, they do have drawbacks. According to Stupar et al, PCMs are mainly effective in thermal applications that have long cycles between hot and cold states [25]. This is due to the fact that PCMs need to dissipate heat into the atmosphere in order to revert back to their original state [25]. This need for rest time could be an issue in situations where ambient temperature is high and the performance demanded of the battery is also high. It is in situations like these that active cooling could prove useful [23]. For vehicle applications, batteries have high power density and operate with high C ratings. The need for an active cooling system is more pronounced.

2.2.2 Active Cooling Methodologies

There are many forms of active cooling from solid state solutions [26] to fluid based solutions (both air and liquid). Chakib developed a thermal management system involving the use of an electro-thermal effect called the Peltier effect in combination with

heat sinks and blowers to cool a battery pack [26]. The Peltier effect is a phenomenon that occurs when two different metals are sandwiched together and a DC current is applied to the sandwich which induces a temperature difference between the two metals [26]. The methodology was found to be highly effective at both reducing the pack temperature and the temperature variation within the pack [26]. However, the system added significant weight and volume to the battery pack [26]. This extra weight could adversely affect the handling and range of an electric vehicle.

There have been researchers working on more conventional active thermal management systems featuring air as the working fluid. Fan et al proposed a cooling system which featured a test stand with a fan on one side of the battery pack and ducts in between each individual battery [27]. The fan forced air through the ducts thus cooling the batteries [27]. The paper explored various combinations of duct thickness, battery arrangement, and flow rates in order to determine the effect each had on both the temperature rise and the temperature variation within each cell [27]. They found that, like many of the other methods, with certain combinations of controllable factors the system was very effective at removing heat from the cells and maintaining near uniform temperature distribution across both individual cells and the pack as a whole [27]. However, volume in electric vehicle battery packs is at a premium with cells packed in as close as possible to obtain optimal capacity. With larger gaps between each cell, the number of cells that can be placed within an EV would probably drop [27].

Another approach to active air cooling for lithium ion batteries was proposed by Mohammadian and Zhang. They developed a pin fin heat sink matrix that increased in

height along the flow path [28]. The methodology was tested using various air temperatures and pin fin configurations [28]. Comparing the results of this study to the previously discussed paper it is evident that this particular methodology is superior in terms of both temperature reduction and temperature variance reduction across both individual cells and the pack as a whole [27],[28]. Even though air based active cooling can be effective there is a limit to how much heat ambient air can absorb. This limit is part of the reason why researchers have also studied liquid based active cooling solutions due to the fact they can absorb more heat than air for a given volume.

An example of liquid cooled systems was proposed by Jin et al and involved the use of liquid cooling plates with oblique fins [29]. The oblique fins were added to facilitate better temperature uniformity [29]. According to the data presented, this methodology seems to be effective for both temperature and temperature variation regulation [29]. However, the researchers did not use an actual lithium ion battery to test this methodology so how it will perform in the field needs to be tested.

Mohammadian et al studied the differences between liquid driven external cooling of a battery and liquid driven internal cooling of a battery through micro-channels in the electrodes [30]. This paper found that the internal cooling method was superior to the external cooling method in both reducing variation in temperature throughout the cell and overall cell temperature [30]. The main drawback of this methodology is the complexity it would add in the manufacturability of such lithium ion battery cells.

2.3 TECHNICAL CHALLENGES

Based on the review of the literature presented in this chapter, it is evident that there are certain areas in both the capacity estimation work and the thermal management work that can be expanded upon. For example, in the literature of capacity estimation and capacity fade prediction it is evident that most research utilizes some form of an equivalent circuit model, which is too simple to capture the capacity loss with respect to electrochemical reactions. In addition, many of the methodologies proposed use highly data driven techniques that require the collection of vast amounts of data. Some of them are also computationally expensive. On the thermal management side, none of the papers reviewed discuss the use of optimal control theory to control active cooling systems. Optimal control theory has been used in many areas to great effect in order to manipulate complex systems in desirable ways while minimizing energy expenditure. In a system like an electric vehicle, efficient operation of active cooling systems could benefit greatly from the integration of optimal control theory.

2.4 PROPOSED WORK

2.4.1 Objectives

1. Develop accurate method to estimate capacity
2. Develop optimally controller cooling system for lithium ion batteries

2.4.2 Thesis Outline

Chapter one discusses the societal need for lithium ion batteries and their development. Chapter two discusses the state of the art of both capacity estimation and thermal management. Chapter three covers the work done to estimate capacity using low order physics based model. Chapter four presents an optimally controlled, fan based thermal management system. Finally, chapter five summarizes the work and proposes ideas for future projects.

Chapter 3: Capacity Estimation

3.1 Overview

Various methodologies where attempted to estimate capacity with mixed results. These include Joint extended Kalman filter, dual extended Kalman filter and Dual Unscented Kalman Filter. This chapter will discuss the results and pitfalls of both these methods and the model itself. In addition, this chapter will explore the use of a physics based model that includes capacity fade statistics created by Prada et al[31] and it will explore a methodology advanced by Hu et al [32].

3.2 Low Order physics based Li-ion Battery

The model used in this work was initially developed by Domenico et al [33]. It was then implemented in Simulink and validated by Sandeep Yayathi [6]. Yayathi's work was then expanded upon by Rehan Refai [34] who added thermal effects to the model and used neural networks to improve the model's accuracy. The Simulink model is shown below.

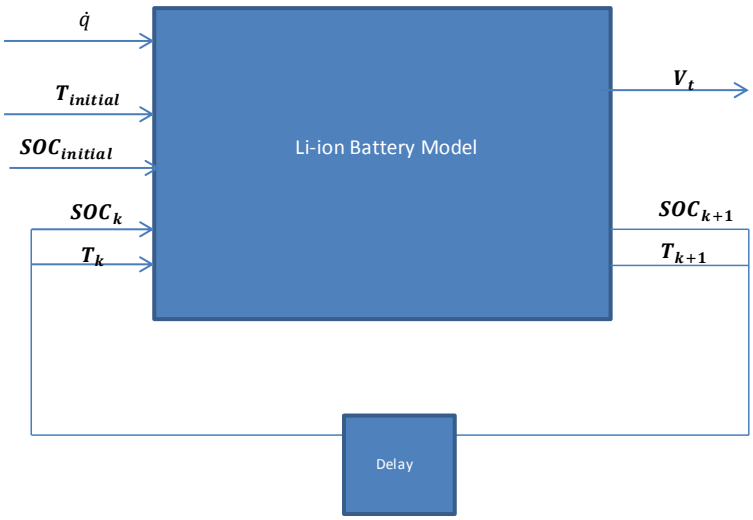

Figure 3.1: Low order physics base li-ion battery model in Simulink [34]

The model shown above has current demand as the input and terminal voltage as the output. It is a two state model with the states being state of charge and battery temperature. All spatial variation has been averaged out of the model [34]. The state and output equations of the model as well as a list of the parameters are shown below.

I Current Demand	k_s Convection coefficient
Q Capacity	$\bar{\eta}_x$ Overpotential
U Thermodynamic potential	$\bar{\phi}_{ex}$ Electrolyte Potential
V Terminal Voltage	R Universal Gas Constant
R_f Film Resistance	F Faraday Constant
T_∞ Ambient Temperature	α_s Active surface area per electrode unit volume
T Battery Temperature	$c_{s_{max_x}}$ Maximum solid concentration of Lithium
M_A Mass of battery	C_p Heat capacity
$\alpha_a \, or \, \alpha_c$ anodic and cathodic electrode reaction charge coefficients	$\bar{c}_{se_p} \, or \, \bar{c}_{se_n}$ Solid concentration at electrode/electrolyte interphase at positive or negative electrode
c_e Concentration of lithium ion in electrolyte	$x_{100\%}, x_{0\%}$ Reference stoichiometry of an electrode
A Electrode plate area	δ_x Electrode thickness

Table 3.1: Parameters and variables for low order physics based model [34]

$$\dot{soc} = -\frac{I}{Q} \tag{3.1}$$

The time rate of change of the state of charge is only a function of the current demand and the capacity which is assumed to be static parameter [34].

$$\dot{T} = \frac{I(U - V + IR_f)}{M_A C_p} - \frac{k_s}{M_A C_p}(T - T_\infty) \tag{3.2}$$

The time rate change in temperature is a function of the heat generated by the battery; which is a function of current demand (I), terminal voltage (V), thermodynamic potential (U) and ohmic resistance (IR), and convection with the air.

$$V(t) = -(\bar{\eta}_p + \bar{\eta}_n) + (\bar{\phi}_{ep} - \bar{\phi}_{en}) + \left(U_p\left(\bar{c}_{se_p}\right) - U_n\left(\bar{c}_{se_n}\right)\right) - R_f I \quad (3.3)$$

The terminal voltage is a function of all the states and is the main measurable quantity of the battery model. Physically, it is actually the function of four phenomena: electrode over-potential$(\bar{\eta}_p + \bar{\eta}_n)$, electrolyte potential $(\bar{\phi}_{ep} - \bar{\phi}_{en})$, thermodynamic potential $\left(U_p\left(\bar{c}_{se_p}\right) - U_n\left(\bar{c}_{se_n}\right)\right)$and ohmic resistance $R_f I$.

The over-potential is the driving force of the battery that induces the movement of ions between electrodes [34]. The equation for this is shown below.

$$\bar{\eta}_x = \frac{RT}{\alpha_a F} \ln\left(\frac{j_x^{-Li}}{2\alpha_s j_{0_x}} + \sqrt{\left(\frac{j_x^{-Li}}{2\alpha_s j_{0_x}}\right)^2 + 1}\right) \quad (3.4)$$

As is evident in the equation above, over potential is a function of exchange current density and the average reaction current. The exchange current density equation is shown below.

$$j_{0_x} = \left(c_{e_x}\right)^{-\alpha_x}\left(c_{s_{max_x}} - c_{se_x}\right)^{\alpha_x}\left(\bar{c}_{se_x}\right)^{-\alpha_x} \quad (3.5)$$

The exchange current density is a function of solid concentration on the electrode which is a function of the stoichiometric ratios of the electrode and the state of charge [34]. The solid concentration ratio is shown below.

$$\bar{c}_{se_x}(t) = [soc(t) * (x_{100\%} - x_{0\%}) + x_{0\%}] * c_{s_{max_x}} \quad (3.6)$$

The average current density is just a function of the electrode volume and the current demand [34].

$$j_x^{-Li} = \frac{I}{A\delta_x} \tag{3.7}$$

The equation for the electrolyte potential is shown below and is a function of the current demand, electrode plate area and the conductivities and thicknesses of the electrodes and separators [34].

$$\left(\bar{\phi}_{ep} - \bar{\phi}_{en}\right) = -\frac{I}{2A}\left(\frac{\delta_n}{k_n^{eff}} + \frac{2\delta_{sep}}{k_{sep}^{eff}} + \frac{\delta_p}{k_p^{eff}}\right) \tag{3.8}$$

The thermodynamic potential is the inherent energy due to the electrodes material and electrical properties and the equations are experimental curve fits that are functions of state of charge that can be found in [34]. The ohmic resistance voltage is the last term of equation 3.3 and is the result of the resistance caused by the growth of the SEI layer [34].

3.3 JOINT EXTENDED KALMAN FILTER

3.3.1 Methodology

The Joint Extended Kalman Filter is a recursive estimation algorithm that is used to estimate the states and parameters of nonlinear systems. The "Joint" comes from the fact that it uses an augmented version of the model with the parameter of interest included (which in our case is capacity). The methodology presented in this work is based on the work done by Plett [35] to estimate state of charge and state of health. However, the implementation described in this chapter uses the physics based model

presented in section 3.2 as opposed to the equivalent circuit model used by Plett [35]. First, initial values for the states, parameters, covariance matrices are chosen. There are three covariance matrices: the covariance for the process noise, the covariance for the measurement noise, and the state covariance. The first two are tunable parameters that greatly affect the performance of the filter [35] and the last one is updated by the algorithm both in time and using measurement information. Once these initial values are set, the states are entered into the model and the Jacobian for the system dynamic equations relative to the states is calculated and then the model is advanced one time step using a runge-kutta algorithm [36]. The runge-kutta algorithm is necessary because the model is a continuous time model while the Joint EKF is a discrete time algorithm. This means that the model must be discretized in order to be compatible with the algorithm and this is where runge-kutta is utilized. The simulation code was assembled using Matlab and Simulink. The code for the JEKF and the other Kalman filter implementations was based on code from Yi Cao [37] and the runge-kutta algorithm and its variants were based on the original by Longoria [38]. A representative model is shown below.

$$\begin{bmatrix} x_{k+1} \\ \theta_{k+1} \end{bmatrix} = \begin{bmatrix} f(x_k, u_k, \theta_k) \\ \theta_k \end{bmatrix} + \begin{bmatrix} w_k \\ r_k \end{bmatrix} \tag{3.9}$$

$$y_k = g(x_k, u_k, \theta_k) + v_k \tag{3.10}$$

In the model above x_k represents the state variable at time step k, u_k represents the input, and θ_k represents the parameter. The state and parameter at the future time step are represented by x_{k+1} and θ_{k+1} respectively. Equation 3.9 represents the state

equations of the system while equation 3.10 represents the output of the system. The process noise terms are w_k and r_k for the states and parameter respectively and v_k is the measurement noise.

Once the Jacobian is calculated, the state covariance ($\Sigma^+_{\hat{x},k-1}$) is updated in time as well using the Jacobian and the process noise covariances Σ_w, Σ_r. The time updated states are then used to calculate the estimated output (in this case voltage). The time update equations are shown below.

$$\hat{X}^-_k = F(\hat{X}^+_{k-1}, u_{k-1}) \quad \text{(state update)} \tag{3.11}$$

$$\Sigma^-_{\hat{x},k} = A_{k-1}\Sigma^+_{\hat{x},k-1}A^T_{k-1} + diag(\Sigma_w, \Sigma_r) \quad \text{(covariance update)} \tag{3.12}$$

$$A_{k-1} = \frac{\partial \mathrm{F}(\hat{X}^+_{k-1}, u_{k-1})}{\partial \hat{X}^+_{k-1}} \qquad C_k = \frac{\partial \mathrm{g}(\hat{X}^-_k, u_k)}{\partial \hat{X}^-_k} \tag{3.13}$$

Once the time update step is complete, the measurement Jacobian, state covariance ($\Sigma^-_{\hat{x},k}$), and the measurement noise covariance are used to calculate the kalman gain. Then the state is corrected using the "innovation term", the difference between the actual measurement and the estimated measurement, and the kalman gain. The state covariance matrix is also updated using the kalman gain and measurement Jacobian. The measurement update equations are shown below.

$$L_k = \Sigma^-_{\hat{x},k}(C_k)^T\left[C_k\Sigma^-_{\hat{x},k}(C_k)^T + \Sigma_v\right]^{-1} \quad \text{(Kalman gain)} \tag{3.14}$$

$$\hat{X}^+_k = \hat{X}^-_k + L_k[\, y_k - \mathrm{g}\left(\hat{X}^-_k, u_k\right)] \quad \text{(state update)} \tag{3.15}$$

$$\Sigma^+_{\hat{x},k} = (I - L_kC_k)\Sigma^-_{\hat{x},k} \quad \text{(covariance update)} \tag{3.16}$$

3.3.2 Results and Analysis

The Joint extended kalman filter was implemented in Simulink and tested using the current demand schedule shown below. The voltage measurement needed for the JEKF was provided by the actual Simulink model of the Lithium ion battery. The initial estimates of the states are shown in the table below. The actual capacity for this simulation is 25920 As and is treated as a constant parameter in this simulation.

Initial SOC=.8	Initial T=280 Kelvin
Initial capacity=20736 As	$\Sigma_{w_{SOC}} = 0.003$ (SOC noise covariance)
$\Sigma_{w_T} = 0.1$ (Temperature noise covariance)	$\Sigma_{r_{Capacity}} = 0.01$ (Capacity noise cov.)
$\Sigma_v = 0.05$ (measurement noise covariance)	$\Sigma^+_{\widehat{soc},k-1} = .0001$ (initial state covariance)
$\Sigma^+_{\hat{T},k-1} = 1000$ (initial state covariance)	$\Sigma^+_{\widehat{Capacity},k-1} = 1.0e5$ (initial state cov.)

Table 3.2: Settings of JEKF

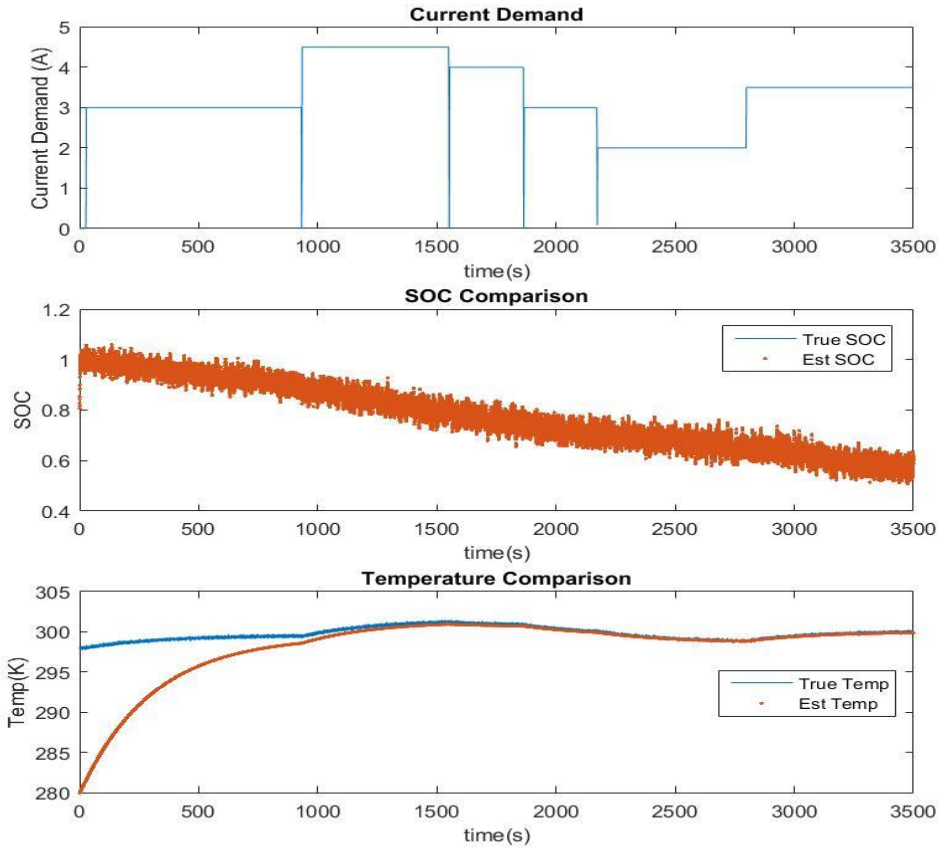

Figure 3.2: Plots for JEKF test

This current demand schedule was selected because it was used in physical battery testing by Rehan [34] and thus is a close representation of what a battery might face in actual operation. The JEKF does a good job of estimating the state of charge and the temperature of the battery but failed to converge on the true capacity value. This is due to the fact that the capacity term does not explicitly exist in the output equation so the algorithm used to calculate the measurement Jacobian returns a zero for that entry of the Jacobian.

3.3.3 Summary

A joint extended Kalman filter was implemented and simulated in order to test its effectiveness in the problem of capacity estimation. Based on the results above, this particular methodology has proven to be ineffective in estimating capacity when coupled with this low order model. This could be due to the fact that capacity does not have an explicit impact on the terminal voltage. This means that pathways to revealing the implicit relationship must be explored. One of the pathways that could accomplish this task is the dual extended Kalman filter.

3.4 Dual Extended Kalman Filter

3.4.1 Methodology

The Dual Extended Kalman Filter is essentially two extended Kalman filters running simultaneously with information exchanged between them. One Kalman filter handles the state estimation and the other handles the parameter estimation. In this implementation, the Jacobian of the measurement function with respect to the parameter is calculated by a recursive derivative function that was hoped would extract the implicit dependence of terminal voltage on capacity. The methodology presented here is based of the work of Hu et al [13]. A diagram showing the structure of the Dual EKF is shown below.

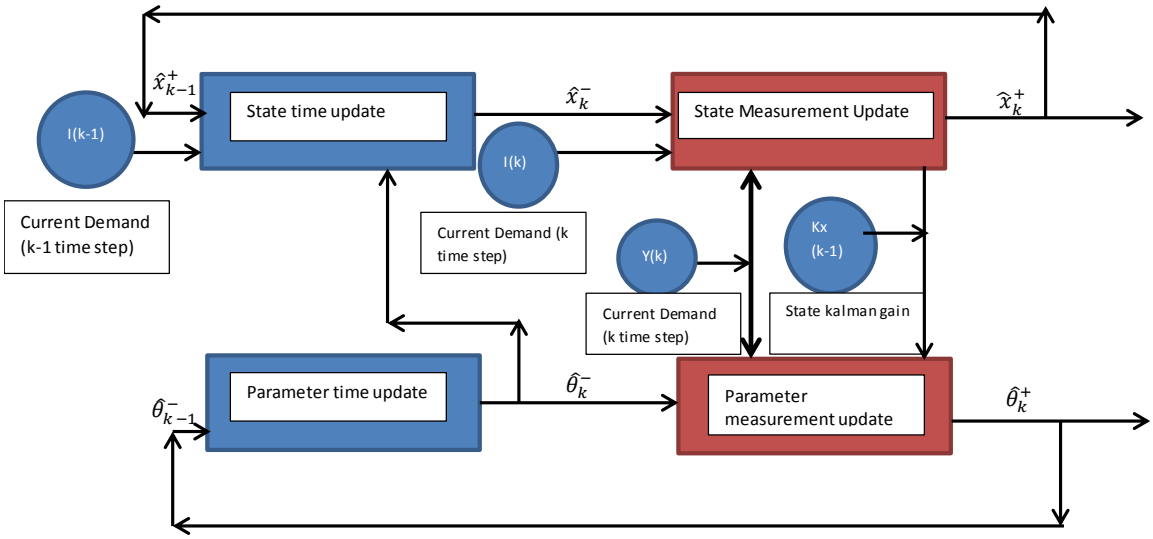

Figure 3.3: Diagram of DEKF [35]

The blue lines that feedback into the state time and parameter time update boxes represent the new estimate of the state or parameter being used to predict the next state or parameter. In order to utilize this method equation 3.9 is altered by removing the parameter as a state and creating a separate state space model of the parameter. The parameter state space system is shown below.

$$\theta_{k+1} = \theta_k + r_k \tag{3.17}$$

$$d_k = g(x_k, u_k, \theta_k) + e_k \tag{3.18}$$

In the above equations r_k and e_k represent the zero mean Gaussian process noise and measurement noise respectively. These equations in conjunction with equations 3.9 and 3.10 are used in the time update step of the duel extended kalman filter. The time update equations are shown below.

Time update for parameter:

$$\hat{\theta}_k^- = \hat{\theta}_{k-1}^+ \tag{3.19}$$

$$\Sigma_{\hat{\theta},k}^{-} = \Sigma_{\hat{\theta},k-1}^{+} + \Sigma_r \tag{3.20}$$

Time update for State:

$$\hat{x}_k^- = f\left(\hat{x}_{k-1}^+, u_k, \hat{\theta}_k^-\right) \tag{3.21}$$

$$\Sigma_{\hat{x},k}^{-} = A_{k-1}\Sigma_{\hat{x},k-1}^{+}A_{k-1}^T + \Sigma_w \tag{3.22}$$

$$A_{k-1} = \frac{\partial \mathrm{f}(\hat{x}_{k-1}^+, u_{k-1}, \hat{\theta}_k^-)}{\partial \hat{x}_{k-1}^+} \tag{3.23}$$

Equations 3.19 and 3.21 are the parameter and state time update equations respectively and equations 3.20 and 3.22 are the covariance time update equations for the parameter and state respectively. Equation 3.23 is the Jacobian for the state subsystem.

The next step in the DEKF methodology is to perform the measurement update step on both the state and the parameter.

Measurement update for state:

$$L_k^x = \Sigma_{\hat{x},k}^{-}(C_k^x)^T\left[C_k^x\Sigma_{\hat{x},k}^{-}(C_k^x)^T + \Sigma_v\right]^{-1} \tag{3.24}$$

$$\hat{x}_k^+ = \hat{x}_k^- + L_k^x[\,y_k - \mathrm{g}\left(\hat{x}_k^-, u_k, \hat{\theta}_k^-\right)] \tag{3.25}$$

$$\Sigma_{\hat{x},k}^{+} = (I - L_k^x C_k^x)\Sigma_{\hat{x},k}^{-} \tag{3.26}$$

$$C_k^x = \frac{\partial \mathrm{g}(\hat{x}_k^-, u_k, \hat{\theta}_k^-)}{\partial \hat{x}_k^-} \tag{3.27}$$

The equations shown above mirror the ones of the JEKF. Equation 3.24 is the Kalman gain calculation, 3.25 is the state measurement update, 3.26 is the state covariance update and 3.27 is the state measurement Jacobian.

Measurement update for parameter:

$$L_k^{\theta} = \Sigma_{\hat{x},k}^{-}(C_k^{\theta})^T \left[C_k^{\theta}\Sigma_{\hat{x},k}^{-}\left(C_k^{\theta}\right)^T + \Sigma_e\right]^{-1} \tag{3.28}$$

$$\hat{\theta}_k^{+} = \hat{\theta}_k^{-} + L_k^{\theta}[\, y_k - \mathrm{g}(\hat{x}_k^{-}, u_k, \hat{\theta}_k^{-})] \tag{3.29}$$

$$\Sigma_{\hat{\theta},k}^{+} = (I - L_k^{\theta} C_k^{\theta})\Sigma_{\hat{\theta},k}^{-} \tag{3.30}$$

$$C_k^{\theta} = \frac{\mathrm{dg}(\hat{x}_k^{-}, u_k, \hat{\theta}_k^{-})}{\mathrm{d}\hat{\theta}_k^{-}} = \frac{\partial \mathrm{g}(\hat{x}_k^{-}, u_k, \hat{\theta}_k^{-})}{\partial \hat{\theta}_k^{-}} + \frac{\partial \mathrm{g}(\hat{x}_k^{-}, u_k, \hat{\theta}_k^{-})}{\partial \hat{x}_k^{-}} \frac{\mathrm{d}\hat{x}_k^{-}}{\mathrm{d}\hat{\theta}_k^{-}} \tag{3.31}$$

$$\frac{\mathrm{d}\hat{x}_k^{-}}{\mathrm{d}\hat{\theta}_k^{-}} = \frac{\partial \mathrm{f}(\hat{x}_{k-1}^{+}, u_{k-1}, \hat{\theta}_k^{-})}{\partial \hat{\theta}_k^{-}} + \frac{\partial \mathrm{f}(\hat{x}_{k-1}^{+}, u_{k-1}, \hat{\theta}_k^{-})}{\partial \hat{x}_{k-1}^{+}} \frac{\mathrm{d}\hat{x}_{k-1}^{+}}{\mathrm{d}\hat{\theta}_k^{-}} \tag{3.32}$$

$$\frac{\mathrm{d}\hat{x}_{k-1}^{+}}{\mathrm{d}\hat{\theta}_{k-1}^{-}} = \frac{\mathrm{d}\hat{x}_{k-1}^{-}}{\mathrm{d}\hat{\theta}_{k-1}^{-}} - L_k^{x} \frac{\mathrm{dg}(\hat{x}_{k-1}^{-}, u_{k-1}, \hat{\theta}_{k-1}^{-})}{\mathrm{d}\hat{\theta}_{k-1}^{-}} \tag{3.33}$$

The parameter measurement update equations are similar to the state update equations except for the measurement Jacobian which is represented by equations 3.31 through 3.33. These equations are recursive in nature and represent a back propagation of the states and parameters through time [13] that is necessary because the effect of past parameters on the present must be reflected in the Jacobian.

3.4.2 Results and Analysis

The Dual extended Kalman filter was implemented in Simulink and simulated. The voltage measurement needed for the DEKF was provided by the actual Simulink model of the Lithium ion battery. The parameters used for the DEKF are shown below.

Initial SOC=.8	Initial T=280 Kelvin
Initial capacity=20736 As	$\Sigma_{w_{SOC}} = 0.003$ (SOC noise covariance)
$\Sigma_{w_T} = 0.1$ (Temperature noise covariance)	$\Sigma_{e_{Capacity}} = 0.01$ (Capacity noise cov.)
$\Sigma_v = 0.05$ (measurement noise covariance)	$\Sigma^+_{\widehat{soc},k-1} = .0001$ (initial state covariance)
$\Sigma^+_{\hat{T},k-1} = 1000$ (initial state covariance)	$\Sigma^+_{\widehat{Capacity},k-1} = 1.0e5$ (initial param. cov.)

Table 3.3: Settings for DEKF

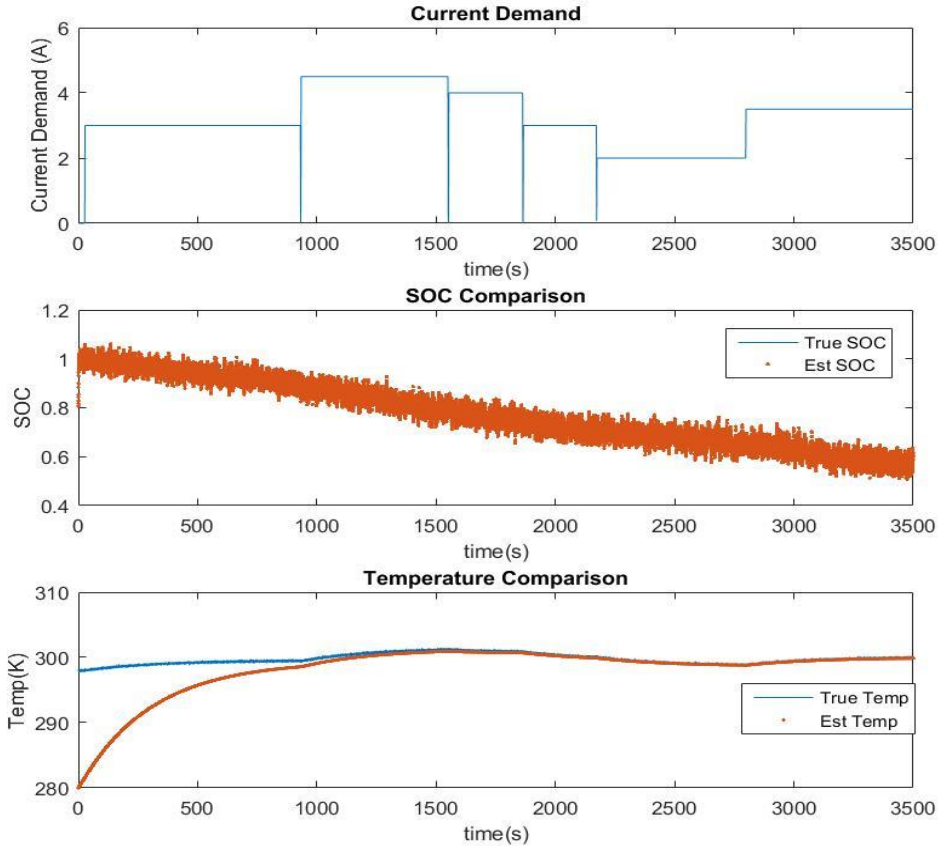

Figure 3.4: Plots for DEKF results

Similar to the JEKF, the DEKF does a good job of quickly and accurately estimating the state of charge and temperature of the battery while the estimate the capacity failed to converge. This problem could be caused by the fact that the first term in equation 3.31 is zero because capacity does not have an explicit effect on the terminal voltage. While the other terms in equations 3.31 through 3.33 have non-zero values, their values are quite small and can effectively be thought of as zero.

3.4.3 Summary

Based on the results from both the JEKF and DEKF simulations, it is evident that the relationship between terminal voltage and capacity cannot be learned through Jacobian based methodologies. Therefore, the next logical step is to apply an estimation method that does not require the calculation of Jacobians like the dual unscented kalman filter.

3.5 Dual Unscented Kalman Filter

3.5.1 Methodology

After the failure of the DEKF it was decided that a DUKF should be attempted. The inspiration for this decision is the work by Qiuting et al where they applied a DUKF to the estimation of state of health and state of charge [21]. The DUKF is essentially the kalman filter combined with the unscented transformation [39]. In this transformation a set of points are calculated that represent the distribution of any Gaussian random variable [39]. These points and associated weights are used to perform time updating and

measurement updating of the states and covariance's [39]. The main benefits include the elimination of Jacobians to calculate and improved accuracy [39]. The dual unscented kalman filter has the same structure as the dual extended kalman filter where there are two filters communicating with each other with one for the states and the other for the parameters [39]. The methodology presented in this work for implementing the DUKF was based on work by Wan and Merwe [39].

Equations for state filter:

Sigma point calculation:

$$X_{k-1} = [\,\hat{x}_{k-1},\, \hat{x}_{k-1} + \gamma\sqrt{P_{k-1}}\,,\, \hat{x}_{k-1} - \gamma\sqrt{P_{k-1}}\,\,] \tag{3.34}$$

$$\gamma = \sqrt{(L+\lambda)} \tag{3.35}$$

L=Dimension of state vector

$$\lambda = \alpha^2(L+\kappa) - L \tag{3.36}$$

$\alpha\ and\ \kappa$ are scaling parameters

State Time Update equations:

$$X_{k|k-1} = F[\,X_{k-1}, u_{k-1}] \tag{3.37}$$

$$\hat{x}_k^- = \sum_{i=0}^{2L} W_i^{(m)}\, X_{i,k|k-1} \tag{3.38}$$

$$W_0^{(m)} = \lambda/(L+\lambda) \tag{3.39}$$

$$W_i^{(m)} = W_i^{(c)} = 1/\{2(L+\lambda)\} \tag{3.40}$$

Covariance time update equation:

$$P_k^- = \sum_{i=0}^{2L} W_i^{(c)}[\,X_{i,k|k-1} - \hat{x}_k^-][\,X_{i,k|k-1} - \hat{x}_k^-]^T + R^v \tag{3.41}$$

$$R^v = process\ noice\ covariance$$

$$W_0^{(c)} = \frac{\lambda}{L+\lambda} + (1 - \alpha^2 + \beta) \tag{3.42}$$

$$\beta = scaling\ parameter$$

Measurement Calculation:

$$Y_{k|k-1} = H[\,X_{k|k-1}] \tag{3.43}$$

$$\hat{y}_k^- = \sum_{i=0}^{2L} W_i^{(m)} Y_{k|k-1} \tag{3.44}$$

First, the sigma points are calculated using equations 3.34 through 3.36. The number of sigma points is equal to the number of states multiplied by two plus one. In the case of the battery model used in this work, five sigma points will be calculated. This means that in equation 3.34, the second and third terms are repeated once. Once the sigma points are calculated, equations 3.37 through 3.44 are used to perform the time update of the states and covariance and to estimate the output. Once the time update step is complete, the measurement update process is initiated.

$$P_{\hat{y}_k \hat{y}_k} = \sum_{i=0}^{2L} W_i^{(c)} [\,Y_{i,k|k-1} - \hat{y}_k^-][\,Y_{i,k|k-1} - \hat{y}_k^-]^T + R^n \tag{3.45}$$

R^n=measurement covariance

$$P_{x_k \hat{y}_k} = \sum_{i=0}^{2L} W_i^{(c)} [\,X_{i,k|k-1} - \hat{x}_k^-][\,Y_{i,k|k-1} - \hat{y}_k^-]^T \tag{3.46}$$

$$K_k = P_{x_k \hat{y}_k} [P_{\hat{y}_k \hat{y}_k}]^{-1} \tag{3.47}$$

$$\hat{x}_k = \hat{x}_k^- + K_k (y_k - \hat{y}_k^-) \tag{3.48}$$

$$P_k = P_k^- - K_k P_{\hat{y}_k \hat{y}_k} K_k^T \tag{3.49}$$

Equations 3.45 and 3.46 calculate the covariance of the measurement estimate and the measurement with respect to the state respectively. Then equation 3.47 uses those two results to calculate the kalman gain, which is then used to update the state estimate (3.48) and the covariance estimate (3.49).

The equations for the parameter UKF are similar to that of the state UKF and are shown below.

Parameter Time updates equations:

$$\widehat{w}_k^- = \widehat{w}_{k-1} \tag{3.50}$$

$$P_{w_k}^- = P_{w_k} + R_{k-1}^r \tag{3.51}$$

R_{k-1}^r=Process noise covariance

$$W_{k|k-1} = [\ \widehat{w}_k^-\ , \widehat{w}_k^- + \gamma\sqrt{P_{w_k}^-}\ , \widehat{w}_k^-\ - \gamma\sqrt{P_{w_k}^-}\ ] \tag{3.52}$$

$$D_{k|k-1} = G[x_k, W_{k|k-1}] \tag{3.53}$$

$$\hat{d}_k = \sum_{i=0}^{2L} W_i^{(m)}\, D_{i,k|k-1} \tag{3.54}$$

Equation 3.50 is the time update equation for the parameter. It is in this form because the assumption is that the parameter does not vary much on the short time scale so it is assumed to be relatively static [39]. Equation 3.51 is the time update for the parameter covariance, 3.52 is the calculation of the sigma points and 3.53 and 3.54 are used to calculate the output estimate.

Measurement Update equations:

$$P_{\hat{d}_k \hat{d}_k} = \sum_{i=0}^{2L} W_i^{(c)}[\ D_{i,k|k-1} - \hat{d}_k^-][\ D_{i,k|k-1} - \hat{d}_k^-]^T + R^e \tag{3.56}$$

R^e=measurement covariance

$$P_{w_k d_k} = \sum_{i=0}^{2L} W_i^{(c)} [\, W_{i,k|k-1} - \hat{w}_k^-][\, D_{i,k|k-1} - \hat{d}_k^-]^T \quad (3.57)$$

$$K_k = P_{w_k d_k} [P_{\hat{d}_k \hat{d}_k}]^{-1} \quad (3.58)$$

$$\hat{w}_k = \hat{w}_k^- + K_k (d_k - \hat{d}_k^-) \quad (3.59)$$

$$P_{w_k} = P_{w_k}^- - K_k P_{\hat{d}_k \hat{d}_k} K_k^T \quad (3.60)$$

Similar to the state measurement update step, equation 3.56 is the covariance of the measurement. Equation 3.57 is the covariance between the measurement and the parameter. Equation 3.58 is the kalman gain calculation with 3.59 and 3.60 being the measurement update equations for the parameter and covariance respectively.

3.5.2 Results and Analysis

The DUKF was implemented in Simulink with the model and then simulated using the current demand schedule from figure 2. The parameters used for the filter are shown below

Initial SOC=.8	Initial T=280 Kelvin
Initial capacity=20736 As	$R^v{}_{SOC} = 0.003$ (SOC noise covariance)
$R^v{}_T = 0.1$ (Temperature noise covariance)	$R^r = 0.01$ (Capacity noise cov.)
$R^n = R^e = 0.05$ (measurement noise cov.)	$P_{k-1,soc} = .0001$ (initial state covariance)
$P_{k-1,T} = 1000$ (initial state covariance)	$P_{w_{k-1}} = 1.0e5$ (initial state cov.)

Table 3.4: Settings for DUKF

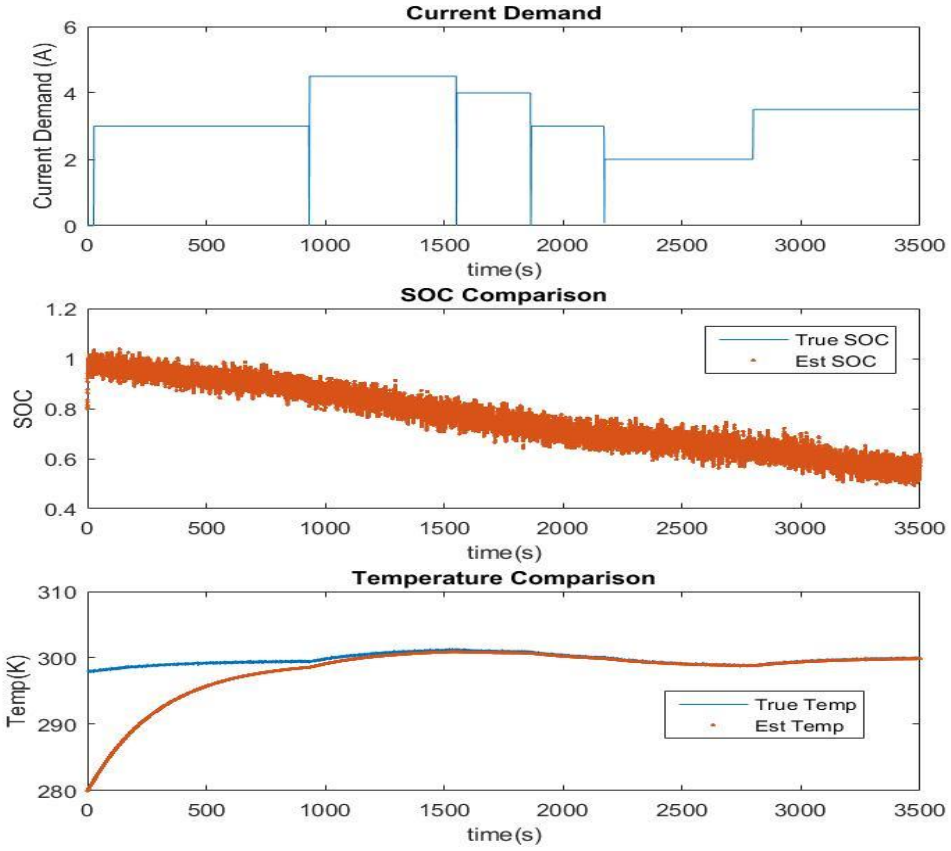

Figure 3.5: Plots for DUKF

The results of this simulation are similar to those of the JEKF and the DEKF in that the state of charge and temperature are well estimated while the capacity estimation fails to converge. This failure to converge is probably due to the same mechanism that caused the other two methodologies to fail: poor observance of capacity through terminal voltage [13].

3.5.3 Summary

After all the various simulations, it is evident that the current combination of this model and the non-linear kalman filter will not produce an accurate estimate of capacity. Based on this realization other methodologies that consider the capacity fade as a state need to be explored.

3.6 AUGMENTED BATTERY MODEL WITH CAPACITY FADE PHYSICS

3.6.1 Methodology

A new modeling method is proposed in this section. The battery model was augmented to include solid electrolyte interphase (SEI) growth and capacity fade physics based on work done by Prada et al [31]. This work focuses on modeling solid electrolyte interphase growth and its effects on capacity fade, film resistance and anode porosity [31]. This model differs from the one that was used in the previous sections in that the capacity is now a state that varies slowly in time as opposed to a static parameter which was the case in Rehan's model. This model was implemented into an Unscented kalman filter in an attempt to estimate capacity. A list of the parameters and the equations are shown below.

E_{a_k} Activation Energy of side reaction rate constant	θ_n^s State of charge
k_f' Solvent reduction Kinetic constant	$R_{s,n}$ Particle radius of negative electrode active particles
β Charge Transfer Coefficent	$\varepsilon_{s,n}$ Active material volume fraction
T_{ref} Reference temperature for Arrehnius equation	M_{SEI} SEI layer molar mass
δ_{SEI} Thickness of SEI layer	ρ_{SEI} SEI layer density
κ_{SEI} Conductivity of SEI layer	$\varepsilon_{f,n}$ filler volume fraction
S_n Active surface area of negative electrode	$c_{s,n,max}$ Maximum solid concentration of Lithium

Table 3.5: Parameters for SEI equations [31]

The main driving force for the SEI growth process is the current density of the SEI formation reaction [31]. This equation is shown below.

$$i_s = -i_s^0 \exp\left(-\frac{E_{a_k}}{R}\left(\frac{1}{T}-\frac{1}{T_{ref}}\right)\right)\exp\left(\left(\frac{\beta F}{RT}\right)*\left(\frac{\delta_{SEI}}{\kappa_{SEI}}\right)*\left(\frac{I}{S_n}\right)\right)\exp\left(-\frac{\beta F}{RT}\left(\phi_{s,n}-U_s\right)\right) \tag{3.61}$$

The first term in the equation is the exchange current density which is a function of state of charge [31] and which is represented by the following equation.

$$i_s^0 = 2F k_f' c_{s,n,max}^2 c_{solv}^* (\theta_n^s)^2 \tag{3.62}$$

Another important variable in this equation is the electric potential of the negative electrode ($\phi_{s,n}$) which is subtracted by the thermodynamic equilibrium potential (U_s) of solvent reduction. The relationship between these two terms represents the potential

difference that affects the current density. The equation for the negative electrode potential is shown below.

$$\phi_{s,n} = U_n + \bar{\eta}_n + \frac{\delta_{SEI}}{\kappa_{SEI}} i_t \tag{3.63}$$

$$i_t = \frac{I}{S_n} = \frac{IR_{s,n}}{3\varepsilon_{s,n}\delta_n A} \tag{3.64}$$

In equation 3.63, U_n represents the energy inherent in the negative electrode, $\bar{\eta}_n$ represents the over potential of the negative electrode and the last term represents the potential loss due to the resistance of the SEI layer [31]. Equation 3.64 is the total current density which is a function of the electrode active surface area (S_n) and the current demand (I) [31].

The current density of the SEI growth process is central to all the phenomena that contribute to capacity fade and the effects of capacity fade.

$$\frac{d}{dt} Q_s = S_n i_s \tag{3.65}$$

$$Q_{s,init} = \varepsilon_{s,n} F \delta_n A c_{s,n,max} |x_{100\%} - x_{0\%}| \tag{3.66}$$

Equation 3.63 represents the capacity fade mechanism of the battery with equation 3.66 representing the initial condition [31]. The capacity fade equation is a representation of how the chemical processes of SEI growth affect the electrical properties of the battery.

Another variable that depends on this current density is the SEI thickness the dynamic equation for which is shown below.

$$\frac{d\delta_{SEI}}{dt} = -\frac{i_s M_{SEI}}{2F\rho_{SEI}} \tag{3.67}$$

The SEI resistance and the electrolyte volume fraction of the negative electrode are also functions of this current density. The equations for both of these parameters are shown below.

$$\frac{dR_{SEI}}{dt} = -\frac{i_s M_{SEI} R_{s,n}}{6F\rho_{SEI}\,\varepsilon_{s,n}\delta_n A\kappa_{SEI}} \text{ or } R_{SEI}(t) = \frac{\delta_{SEI}(t)}{\kappa_{SEI} S_n} \tag{3.68}$$

$$\frac{d\varepsilon_{e,n}}{dt} = \frac{i_s M_{SEI} 3\varepsilon_{s,n}}{2F\rho_{SEI}\,R_{s,n}} \text{ or } \quad \varepsilon_{e,n}(t) = 1 - \varepsilon_{f,n} - \varepsilon_{s,n}\left(1 + \frac{3\delta_{SEI}(t)}{R_{s,n}}\right) \tag{3.69}$$

Equations 3.61 through 3.69 were implement into the model with the parameters found in the Prada et al paper. All the parameters were defined except for c^*_{solv} which is the concentration of solvent at the interphase between the negative electrode and SEI [31]. This parameter was treated as an arbitrary term which was tuned via trial and error to roughly mimic the capacity fade results presented by Prada et al. The use of more sophisticated techniques to tune this parameter will be left to future work. Once the model was augmented, an unscented kalman filter (based on the state UKF equations presented in section 3.5) was applied in order to estimate capacity, SOC, Temperature and SEI thickness.

3.6.2 Results and Analysis

The results for the simulated augmented model with the UKF are shown below. The same current demand was used in this simulation as was used in all others. The initial estimates of the states are shown below.

Initial SOC=.8	Initial T=280 Kelvin
Initial capacity=20736 As	$R^v{}_{SOC} = 0.003$ (SOC noise covariance)
$R^v{}_T = 0.1$ (Temperature noise covariance)	$R^v{}_{capacity} = 200$ (Capacity noise cov.)
$R^n = 0.05$ (measurement noise cov.)	$P_{k-1,soc} = .001$ (initial state covariance)
$P_{k-1,T} = 1000$ (initial state covariance)	$P_{k-1,capacity} = 1.0e5$ (initial state cov.)
Initial SEI thickness= 5e-7 m	$P_{k-1,SEI\ thickness} = R^v{}_{SEI} = 1e-12$

Table 3.6: Settings for Augmented model UKF

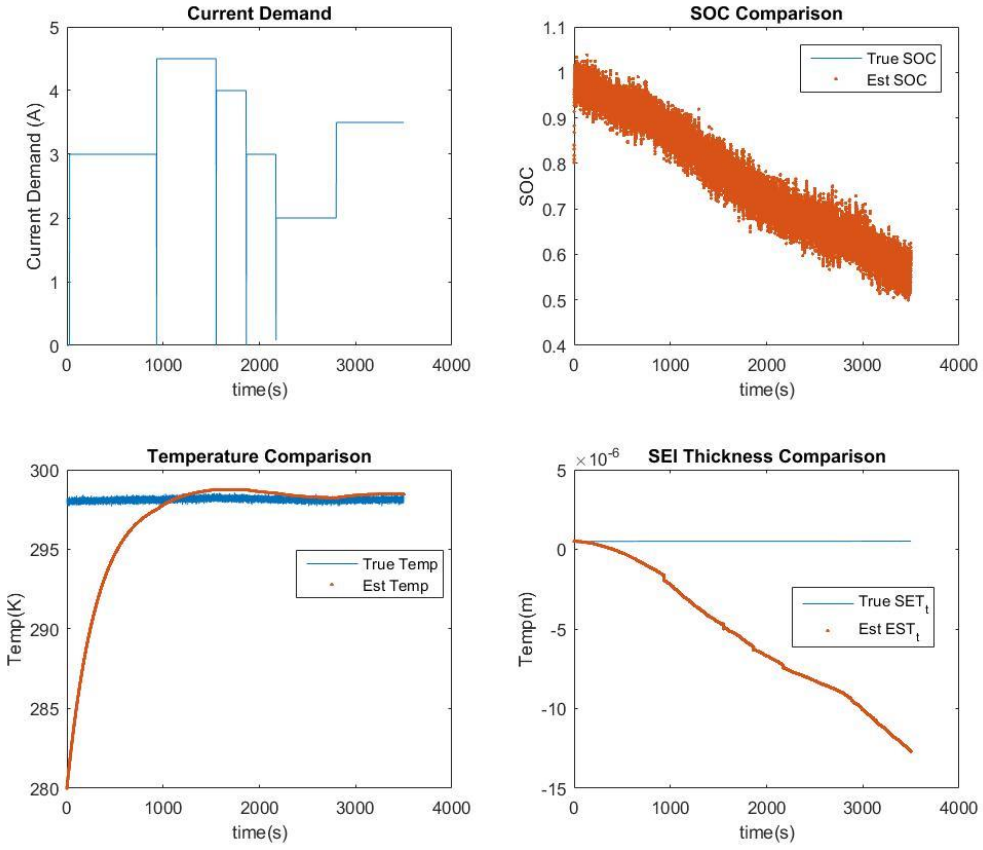

Figure 3.6: Plots of UKF with Augmented model

The results above are similar to what has been shown with previous simulations: the state of charge and temperature are strongly observable from the terminal voltage while the capacity and SEI thickness are basically unobservable. The cause of the capacity observability lies with its weak correlation to the terminal voltage [13]. For the SEI thickness, its un-observability is probably due to the fact that the terms that contain the SEI thickness state in equation 3.61 actually cancel themselves out.

3.6.3 Summary

Augmenting the model with SEI growth physics did little to solve the underlying problem of estimating capacity. This failure let to a fundamental rethinking of how to estimate capacity, which leads to the next methodology.

3.7 INVERSE COULOMB COUNTING METHOD

3.7.1 Methodology

This section will introduce an augmented version of a methodology developed by Hu et al to estimate battery capacity using a rearrangement of the coulomb counting formula to calculate capacity from state of charge and current [32]. The equation used to accomplish this is shown below.

$$C_k = \frac{\int_{t_k}^{t_{k+L}} i(t)dt}{SOC_{k+L} - SOC_k} \tag{3.70}$$

This methodology was tested in Simulink using an EKF that utilized the voltage readings it was receiving from the more complete Prada et al model discussed in the previous section. The SOC from the EKF was then fed into a version of equation shown

above that had a running sum of the current and kept one SOC value steady while the other varied. After an hour the running sum was reset and the steady SOC value was updated. This long summation is necessary to ensure that the current sum is allowed to settle [32]. After a long delay, the value output by equation 3.70 was then passed through a filter of sorts that capped the values at the nominal value on the high end (7.2 Ah) and at 80% of the nominal capacity value at the low end. Then these values were averaged over the number of remaining samples in order to average out any variance and obtain a single representative value for the capacity. This capacity value is then fed back into the EKF model.

3.7.2 Contribution to Field

The methodology presented here differs from the one presented by Chao Hu et al in several ways. One way is that Chao Hu et al uses a simple, equivalent circuit model at the heart of his work while we are using a more sophisticated and detailed low order physics based model. Also, there are various noise reducing methodologies that have been implemented to "smooth" out the capacity estimation that are not present in the work presented by Chao Hu et al.

3.7.3 Simulation Results and Analysis

A battery of simulations was run to explore how the methodology performed under different current demands. The model presented by Prada et al [31] was treated as

the “true” battery and the model created by Rehan [34] was used in the Extended kalman filter. The results are shown below.

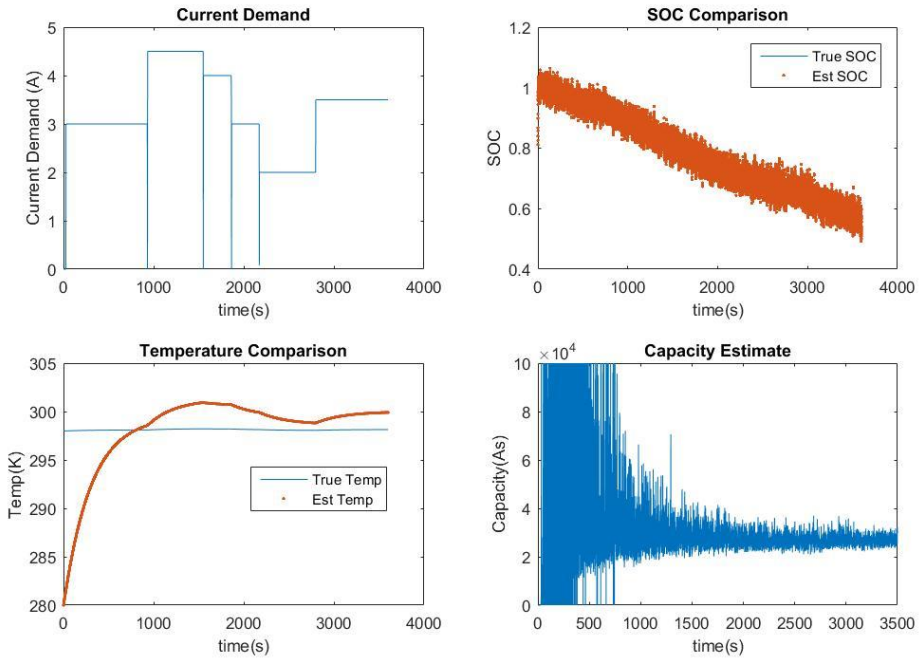

Figure 3.7: Plots for Inverted method test one

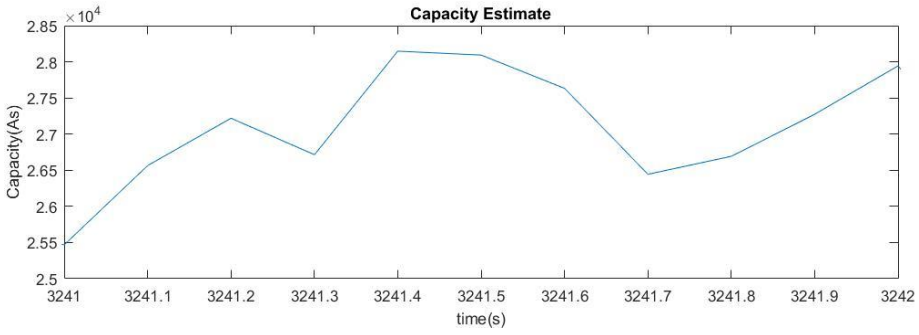

Figure 3.8: Zoomed in capacity plot for test one

The current demand which served as the disturbance input for this simulation shown on the top left hand corner of figure 3.7 was chosen because it represents a normal

current profile for a device using a Lithium ion battery. It is evident from the data that the method does a reasonable job at estimating capacity at every time step. The initial spikes on the bottom right graph of figure 3.7 are due to the current sum not being large enough to dampen out the heavy fluctuations in the state of charge estimate [32]. These spikes are the reason that the average value of the capacity for the hour is only calculated based on the last 80% of instantaneous capacity estimate data. The average calculated for this test was about 25412 As which is about a 1.96% difference from the nominal capacity value of 25920 As (7.2Ah). Based on these results it is evident that this methodology is capable of handling moderately varying current loads. It is also evident that the EKF produced a relatively accurate estimate of state of charge and temperatures. The slight difference between the estimated temperature and the actual temperature is due to physics within the "true" battery model that the model being used in the EKF doesn't capture [31].

The next test explores how the estimation algorithm handles a current demand schedule with pulse discharge curves. This test was designed to observe how the algorithm handles relatively rapid changes in the current demand and state of charge. The results are shown below.

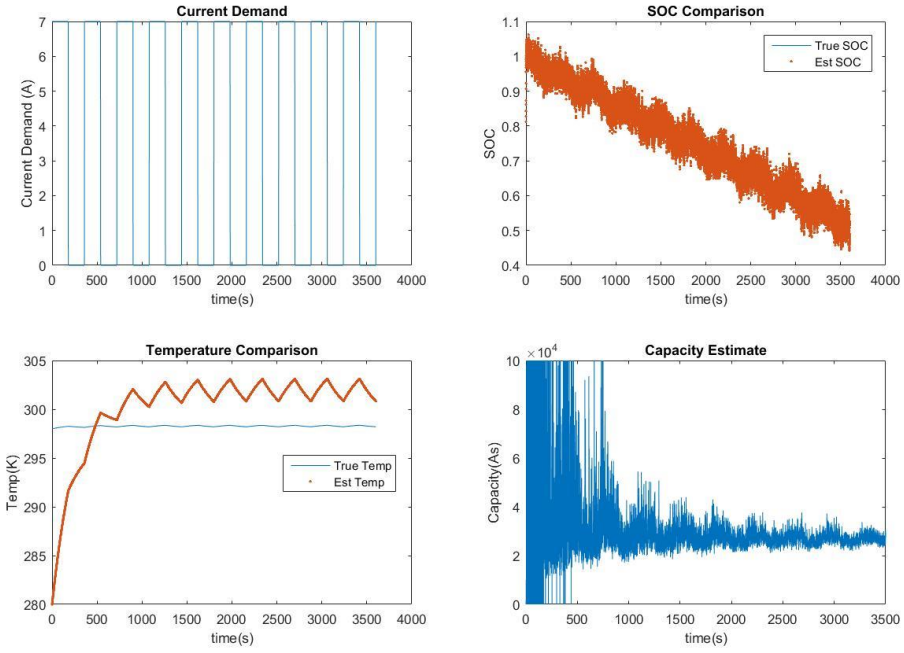

Figure 3.9: Plots for Inverted method test two

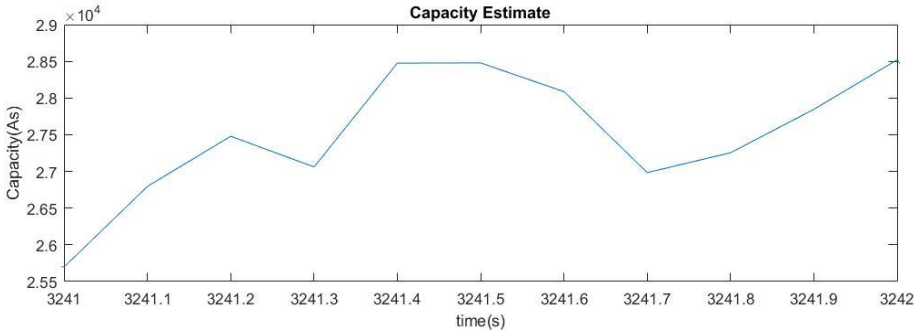

Figure 3.10: Zoomed in capacity plot for test two

Despite the more aggressive current demand, the results for the capacity estimation are similar to the results produced from the first test. This is further proven by the average value (25388 As) which is only 2.05% lower than the nominal capacity. This

data also shows that this methodology can produce relatively accurate capacity estimation in the presence of rapidly changing current demand.

The third test uses a current demand schedule that includes both rapid charge and discharge cycles. This test is meant to simulate actions like regenerative breaking on electric vehicles. The results are shown below.

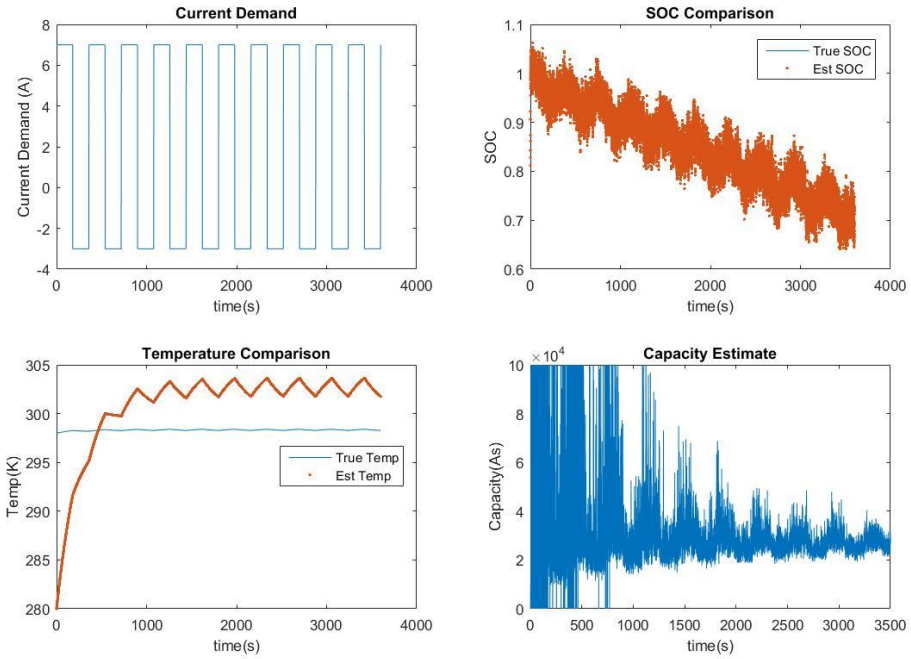

Figure 3.11: Plots for Inverted method test three

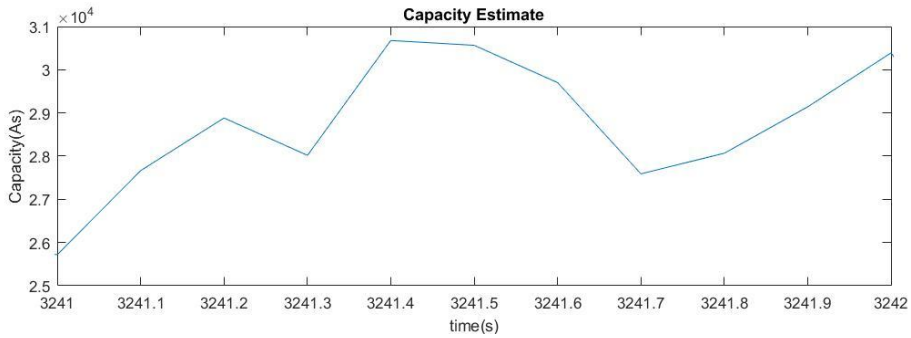

Figure 3.12: Zoomed in capacity plot for test three

Similar to the previous test, this one returned results very similar to the first test with regard to capacity estimation. However, the average capacity estimated was 24858 As which is about 4.4% different from the nominal capacity. This marked difference in error is probably due to the charging portion of the cycles which added extra variance to the state of charge estimate.

The final test was to determine how the algorithm performed at different stages of the batteries life. This was accomplished by repeating each of the test cases outlined in this section with the "true" battery model initialized at 90% of the nominal capacity and then 80% of the nominal capacity. The results are shown below.

	Qinit=7.2Ah (25920As)	Qinit=6.48Ah (23328 As)	Qinit=5.76Ah 20736 As)
Test 1	25412 As (1.96%)	24079 As (3.22%)	22028 As (6.23%)
Test 2	25388 As (2.05%)	24058 As (3.13%)	22029 As (6.24%)
Test 3	24858 As (4.4%)	23748 As (1.80%)	22275 As (7.42%)

Table 3.7: Algorithm accuracy Test results

The table above compares the results of the various tests for a given initial capacity. It is evident that as the capacity is diminished the accuracy of the estimate relative to the actual capacity worsens. This trend could be due to the fact that the upper bound is too high relative to the actual capacity. A possible solution would be to dynamically adjust the bounds based on trends and past data. This way, the resolution of the data set with respect to the range of the data is kept similar. Such a project is left to future work. The only outlier in this trend is the test 3 result for Qinit at 90% nominal capacity. This could be due to the charging portion of the demand schedule.

3.7.4 Summary

In this section the inverse coulomb counting method produced by Chao et al was augmented and tested for accuracy and robustness. This augmented method was found to be relatively accurate when compared to the various non-linear kalman filters which did not converge on any accurate estimate. With regard to robustness, defined by how the algorithm responds to different current demand profiles, it was shown to have variable but adequate performance between the nominal capacity and 90% of the nominal capacity.

3.8 SUMMARY

This section explored various methods to estimate capacity in Lithium ion batteries. It was found that all of the methods which only used non-linear kalman filters were ineffective in accurately estimating capacity. This ineffectiveness was due to their failure to converge to the true value of the capacity which was caused by the limited observability of capacity from voltage [13]. However, from this experimentation a methodology was developed that utilized the state of charge estimate, the inverse of the coulomb counting equation and an averaging algorithm with sampling and saturation limits that can adequately estimate capacity to within two percent accuracy for some cases.

Chapter 4: Thermal Management

The work presented in this chapter is the result of joint venture between the author and a student by the name of Etse Campbell.

4.1 Augmented Model Background

The control objective is to limit the change in battery temperature using linear optimal control theory. The maximum desired change in temperature is about 8 Kelvin. The goal is to minimize the current drawn from the battery, and therefore the power drawn by the fan to control the temperature of the battery.

The physical realization of the thermal control loop is shown below. It is assumed that the battery is contained in a box or chamber with a fan blowing air over the battery which then exits out the other side via a vent. The battery box contains the battery, controller, and fan housing. This is assumed to be a base case that represents a number of battery-load configurations including laptops and electric vehicle systems.

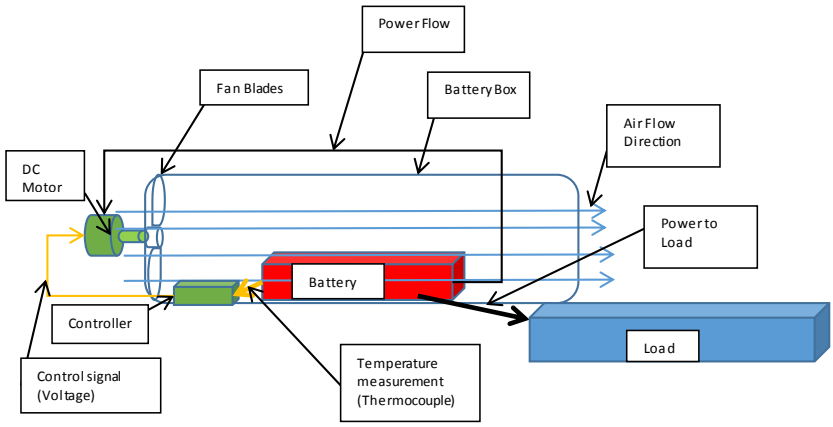

Figure 4.1: Physical Representation of Thermal Management System

This idealized physical representation was then transformed into the Simulink model shown below.

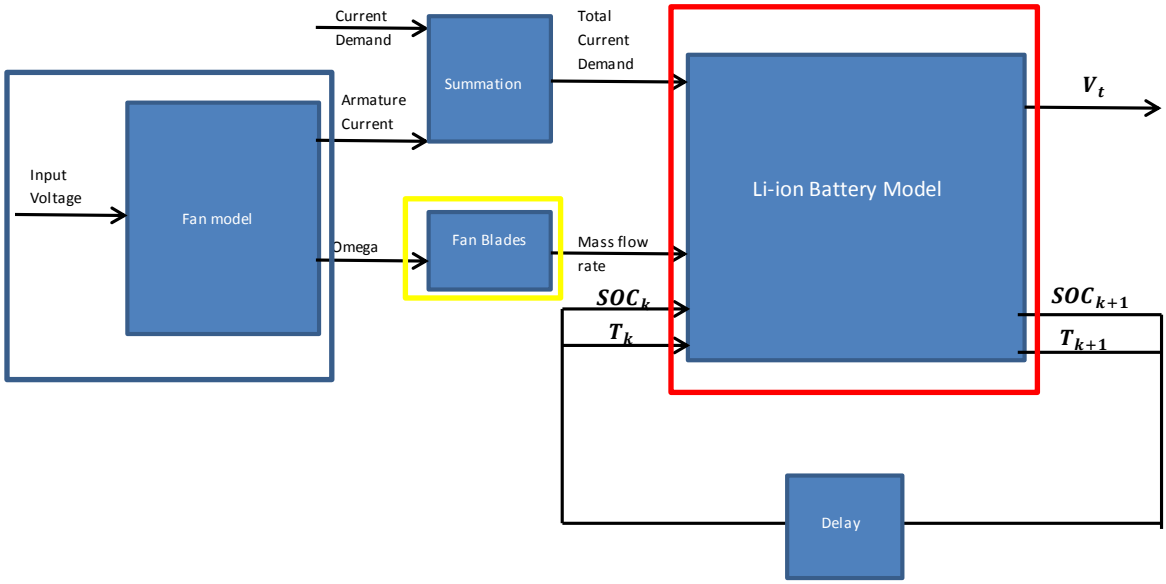

Figure 4.2: Simulink Representation of Thermal Management System

On the right encircled in red is the battery model described in the chapter one with a small change to the thermal subsystem. On the left encircled in blue is the DC motor and fan subsystem which provide forced air cooling to the battery. The fan subsystem is controlled by a voltage and powered by the battery itself. Based on the voltage input, the two-state fan system passes an omega term to the "fan blade" sub system in the yellow box which in turn passes a mass flow rate to the temperature subsystem in the battery model. In addition to the assumptions outlined in chapter one, more assumptions related to the thermal modeling of the battery are outlined below.

- All spatial gradients are averaged out [34]. This assumption holds because the space being considered for the battery box is relatively small (on the order of

10^1 cm) and as such air temperature and density should remain fairly constant.

- Thermally speaking, the battery is treated as a lumped entity [34]
- The current demanded by the battery from the main load is considered a disturbance input due to the fact it is uncontrollable from the perspective of the battery [Dr. Chen].
- Heat transfer is only between battery and air [Dr. Headley]. This means there is no radiation present and minimal conduction between the battery and the box itself [Dr. Headley].
- 1-D flow of Air to eliminate the need for computing convection effects in three dimensions
- Assume convection coefficient (k_s) is only a function of air speed. Typically, the convection coefficient is a function of the difference in temperature between the body and its surroundings. In this model, the difference is not taken into consideration to simplify computations.
- Air within battery cabinet has constant density. In reality, air density changes with space and temperature.

4.1.1 Temperature Subsystem

The temperature subsystem of the original battery model was augmented slightly to account for the convection coefficient's dependence on air velocity. This modification was the result of conversations with Dr. Headley. The equation that represents this dependence is shown below [40].

$$k_s = \mathrm{A} * \left(\frac{\mathrm{k}_f}{L}\right) * (0.664) * (Re)^{.5}(\mathrm{pr})\text{^}(\tfrac{1}{3}) \tag{4.1}$$

$$Re = \frac{\rho * V * L}{\mu} \tag{4.2}$$

This equation assumes that the battery is a flat plate and all heat transfer occurs from the top surface. In equation 4.1, "A" is the surface area of the battery, "Re" is the Reynold's number, and "pr" is the prandtl number. For equation 2.2, rho is the density of air, V is velocity, L is the length of the plate in the direction of flow and mu is the dynamic viscosity of air. Within this application this equation is only valid if the velocity is greater than 0.51 m/s. This is due to the fact that free convection has a convection coefficient of 5 and 0.51 m/s is the velocity at which said coefficient value is achieved via forced convection.

4.1.2 Fan Subsystem

The fan subsystem consists of a DC motor model developed by a member of the University of Michigan [41] and a simple model of a fan blade assembly based on Gorla

and Khan [42]. The state space model of the DC motor and its Simulink incarnation are both shown below.

$$\frac{d}{dt}\begin{bmatrix}\dot{\theta}\\ i\end{bmatrix} = \begin{bmatrix}-\frac{b}{J} & \frac{Kt}{J}\\ -\frac{Kb}{L} & -\frac{R}{L}\end{bmatrix}\begin{bmatrix}\dot{\theta}\\ i\end{bmatrix} + \begin{bmatrix}0\\ \frac{1}{L}\end{bmatrix}V \tag{4.3}$$

Above is a model of a DC fan motor that will be used to drive the fan blades. The input to this model is voltage with the states being armature current and the angular speed of the rotor. The fan blades where designed using the assumption that the axial velocity was constant through the fan which allowed the use of the following equation.

$$C = \frac{U}{\tan(\propto)+\tan(\beta)} \tag{4.4}$$

This equation gives the axial velocity being output from the fan. "U" is the linear rotor speed, alpha is the inlet angle of the air and beta is the exit angle of the air. The diagram of this phenomenon is below.

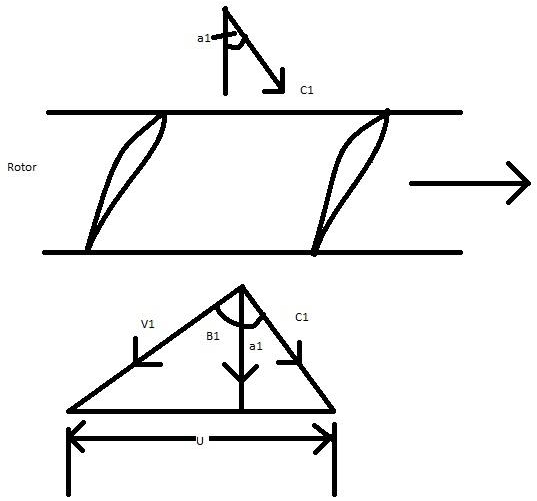

Figure 4.3: Fan velocity diagram [42]

The speed of air due to the fan rotation is C (m/s) with U being the angular speed of the fan multiplied by the mean radius of the fan blade and alpha is the angle of the air flow coming into the fan and beta is the angle of the air flow speed relative to the fan. Alpha and beta are determined by the airfoil design and are assumed to be arbitrary. The assumptions used to model the fan system are listed below along with the physical parameters for the DC motor, fan blades and fan opening.

- Voltage input for DC motor system
- Values given for rotational inertia encompass fan blades
- Axial velocity is constant through fan
- Inlet air velocity equals inlet absolute air velocity ($\alpha = 0°$)

- Exit angle (β angle) of air foil set at 10 degrees
- Mass Flow rate: $\dot{m} = \rho AC$
- Air Density 1.225kg/m^3, A=0.00754 m^2
- U=rm*w with rm being the average radius of the fan blade
- rm=3cm. Rl=5cm and rh=1cm
- The mass moment of inertia was calculated assuming that the hub was a circle and the blades were small flat plates [43]

Below is a table of the DC motor parameters derived from experiments and research conducted by Dr. Victor Yu.

Moment of Inertia of the rotor Moment of Inertia of the fan	Jrotor=0.00261 kg m^2 Jfan=1.896e-6 kg m^2
Motor Viscous Friction constant	B= 0.0268 Nms
Electromotive force constant	Ke= 0.005448102 V/rad/sec
Motor Torque constant	Kt= 0.002053018 Nm/Amp
Electric Resistance	R=1 ohm
Electric Inductance	L=0.5H

Table 4.1: Parameters for DC motor

4.1.3 Contribution to Field

No thermal management system explored in the literature reviewed for this work has used optimal control theory to manage the actuators (fans, pumps, etc). Therefore, the contribution of this work will be the development of an optimally controlled active thermal management system. The system will use a fan as the cooler and the lithium ion battery model as the object to be cooled. The work presented in this thesis represents a base case that provides good insight into how an optimal controller could benefit such thermal management systems.

4.2 OPERATING POINT SELECTION

In order to apply linear control theory to this problem the non-linear system presented above has to be linearized. The linearization process first involved the selection of an operating point. A battery of tests was run in order to determine the effectiveness of the fan for different current draws and to help determine a suitable operating point about which to linearize. The figure 4.4 shows temperature changes for open loop battery operation at different Current Draw Specifications. The current draw specified below the figures is only the current demanded by the battery from a load. It does not include the current drawn from the battery by the motor.

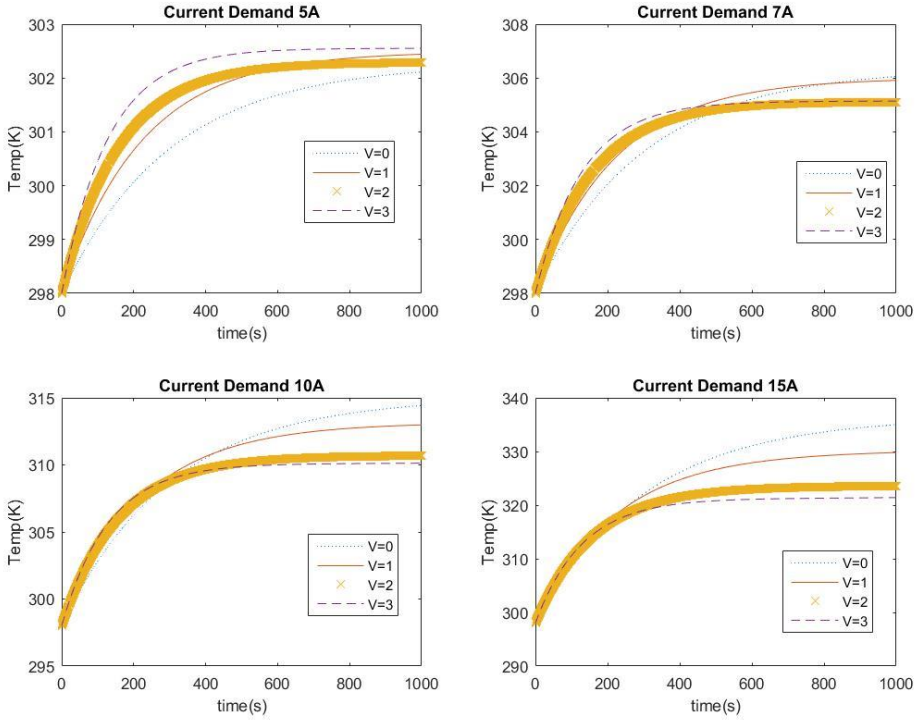

Figure 4.4: Open Loop Test Results

It is evident that at low current demand the fan does not offer much benefit. This is because at low current demands from the main load the fan accounts for a much greater percentage of the overall current demand relative to the load demand. However, it can be seen at higher load demands that the fan action has a significant effect on the temperature of the battery lowering it considerably. Another trend can be seen when comparing the best fan settings for each current demand. For the 5A case, the best setting for the fan is the 2 volt setting. This is probably due to the fact that this setting is a good balance between cooling ability and current draw on the battery. For the 7A case, the best setting is a tie between the 2 and 3 volt settings. However, at the 10A and 15A cases the clear winner is the 3V setting. This is due to the cooling power of the fan being much more prominent than the current the fan was drawing from the battery. Once this testing was completed an operating point was found using the 3 volt curve at 10 amps and taking a snap shot of the simulation at T=500s. This "snapshot" was then run through Simulink's linearization tool box to produce the linear system. This method of finding a linearization point was used because the results are physically realizable. The parameters that characterize the point are shown below.

State of Charge	0.75098
Temperature (kelvin)	309.8647 K
Armature Current (Amps)	2.9091 A
Rotor Speed (rad/s)	16.6763 rad/s

Table 4.2: Operating Point for Linearization

4.3 LINEAR QUADRATIC REGULATOR (LQR) DESIGN AND RESULTS

The first attempt at control was a discrete time infinite time horizon linear quadratic regulator. Its purpose is to drive the states to zero through the most minimal control action possible without preference for a finite time of completion [44]. It accomplishes this task by finding the most optimal gains for state feedback by minimizing a cost function in which the designer outlines the control objectives [44]. The control objectives are represented by three weighting matrices: one for the states, one for the input and one for the final states [44]. These matrices are symmetric and positive semi definite [44] and determine the desired variance of the states and the desired control effort. Using the operating point shown in figure 4.4, a linearized system was developed. This linearized system was used to design the discrete LQR controller using Matlab functions with a sample time of 0.01 seconds. The linearized system and the cost function for the controller are shown below.

$$\begin{bmatrix} \dot{soc} \\ \dot{T} \\ \dot{\omega} \\ \dot{i} \end{bmatrix} = \begin{bmatrix} 0 & 0 & -3.8580e^{-5} & 0 \\ -1.3201e^{-04} & -.0077 & 0.0145 & -0.0028 \\ 0 & 0 & 58.8183 & -10.2607 \\ 0 & 0 & -101.5862 & -0.5535 \end{bmatrix} \begin{bmatrix} soc \\ T \\ \omega \\ i \end{bmatrix} + \begin{bmatrix} 0 \\ 0 \\ 101.5862 \\ 0 \end{bmatrix} [V]$$

$$+ \begin{bmatrix} -3.8580e^{-5} \\ 0.0145 \\ 0 \\ 0 \end{bmatrix} [I] \quad (4.4)$$

$$\begin{bmatrix} V_b \\ T \end{bmatrix} = \begin{bmatrix} .5190 & 0 & 0 & -0.0022 \\ 0 & 1 & 0 & 0 \end{bmatrix} \begin{bmatrix} soc \\ T \\ \omega \\ i \end{bmatrix} + \begin{bmatrix} 0 \\ 0 \end{bmatrix} [V] + \begin{bmatrix} -0.0022 \\ 0 \end{bmatrix} [I] \quad (4.5)$$

The cost function:

$$J = \int_0^\infty \left(\begin{bmatrix} soc \\ T \\ \omega \\ i \end{bmatrix}^T \begin{bmatrix} 1 & 0 & 0 & 0 \\ 0 & 1000 & 0 & 0 \\ 0 & 0 & 1 & 0 \\ 0 & 0 & 0 & 1000 \end{bmatrix} \begin{bmatrix} soc \\ T \\ \omega \\ i \end{bmatrix} + [V]^T (1000)[V] \right) dt \quad (4.6)$$

The first test conducted with this controller was perturbing the battery temperature state by 5 degrees kelvin. The purpose of this experiment is to observe how responsive the LQR is to perturbations and to see how close the controllable states get to zero.

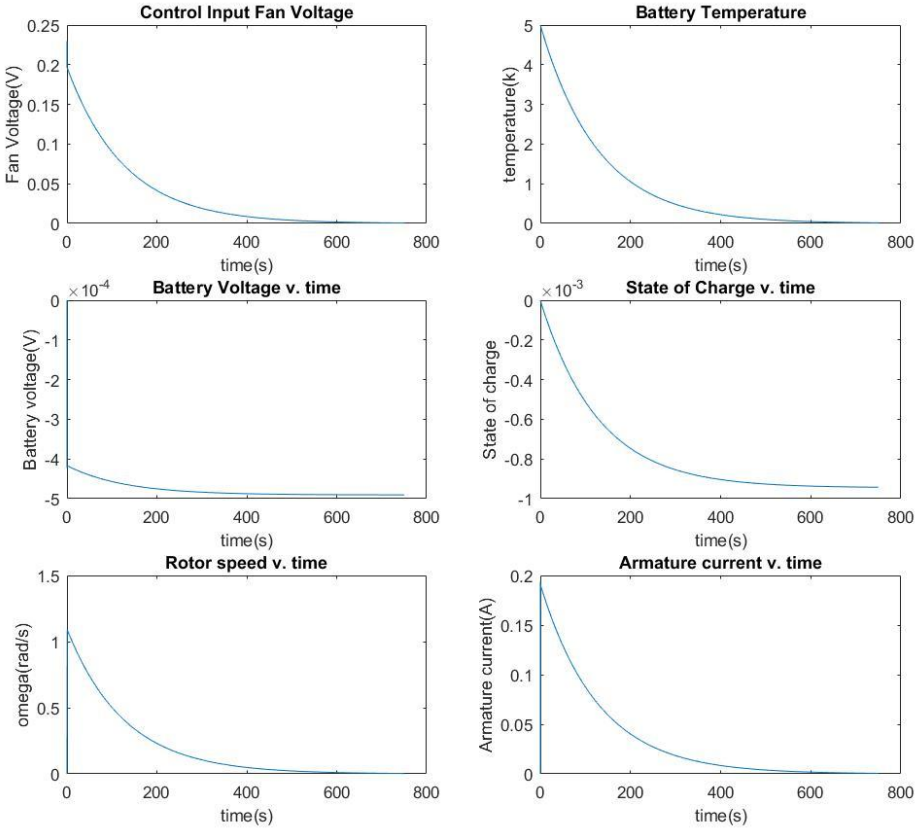

Figure 4.5: Dynamic responses for LQR perturbation test

The results of this test shows that the LQR is effective in regulating variation of the battery temperature back to zero while staying within the voltage and current limits of the DC motor. However, the controller took too long in accomplishing this task in that this operating point would no longer be a valid representation of the actual battery system by the time the temperature reached the zero point. In addition, this test was conducted without perturbation in the current demand which could change numerous times in an actual system during the time window analyzed.

Based on these observations, the following experiment involved a 10% increase in the current demand from 10A to 11A or a delta I of 1 A. In addition, the temperature is perturbed by 0.5 degrees kelvin in order to maintain an assumption of the LQR controller that at least one initial state is nonzero [44]. This was modeled as a step input lasting the duration of the experiment. Now, it should be noted that the infinite horizon LQR was not designed to handle exogenous disturbances [44]; however this experiment is necessary in order to determine the robustness of the controller and to see if it can achieve and maintain a temperature reasonably close to the starting one. The results for this test are shown below.

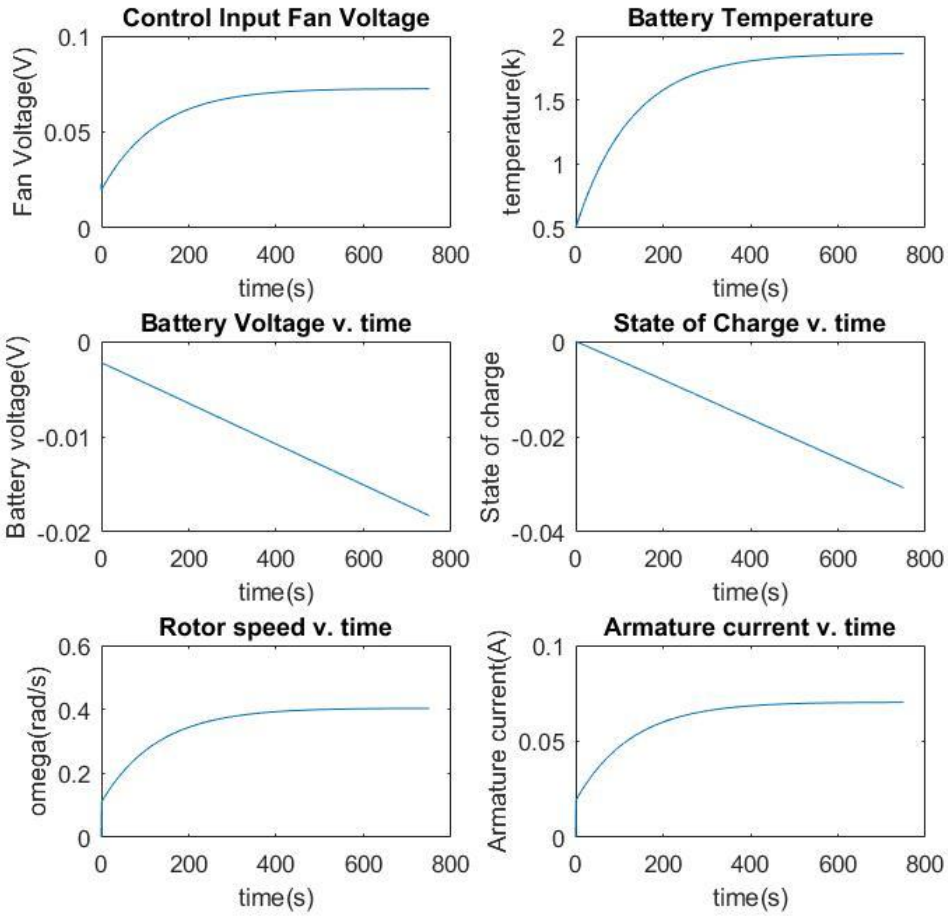

Figure 4.6: LQR w/disturbance responses

It is evident by the dynamic response of the battery temperature that the LQR controller failed to drive the temperature change to zero in the presence of a disturbance. However, it managed to keep the temperature from rising more than 2 degrees kelvin. Similar to the LQR test without disturbance, the response of the controller to the change in temperature is very slow. In fact, both of the controller response times are similar to the response times observed with the open loop cooling experiments. This phenomenon is

probably due to the fact that both the open loop and closed loop systems generate similar air velocities.

4.4 LQR WITH DISTURBANCE REJECTION DESIGN AND RESULTS

As was made evident in the previous section, significant disturbances can eliminate the LQR controller's ability to drive the temperature to zero. Also, while one can manipulate the weighting matrices of the LQR to force the states near zero, this method is not necessarily optimal. Therefore, there needs to be a disturbance rejection mechanism added to the LQR in order to properly mitigate the effect of that disturbance on the temperature.

The disturbance rejection methodology [45] applied in this work splits the model into portions directly affected by the disturbance and those not directly affected by the disturbance in order to facilitate the calculation of a static gain that can be applied to the disturbance creating a new "disturbance rejection" term that can be added to the control input in the hopes of negating its effect [45]. The relevant equations are shown below.

$$\begin{pmatrix} A & B \\ C_e & D_e \end{pmatrix}\begin{pmatrix} \Pi \\ \Gamma \end{pmatrix} + \begin{pmatrix} B_d \\ D_{ed} \end{pmatrix} = 0 \tag{4.7}$$

$$G = \Gamma + K\Pi \tag{4.8}$$

K=gains derived from LQR algorithm

In equation 4.7, the "A" matrix is first 4x4 matrix in equation 4.4 and represents the system parameters. The "B" matrix is the matrix associated with the controllable input (fan voltage) in equation 4.4. Similarly, the B_d matrix is associated with the disturbance

input "I" in equation 4.4. The C_e matrix represents the second row of the C matrix in equation 4.4 and describes how the states relate to the control variable. Finally, the D_e matrix and the D_{ed} matrix relate the control input and the disturbance input to the output respectively.

The disturbance rejection term was added to the original LQR control input and the whole system was simulated in MATLAB. The same parameters used in the previous simulation with disturbance were used here. The results of the simulation are shown below.

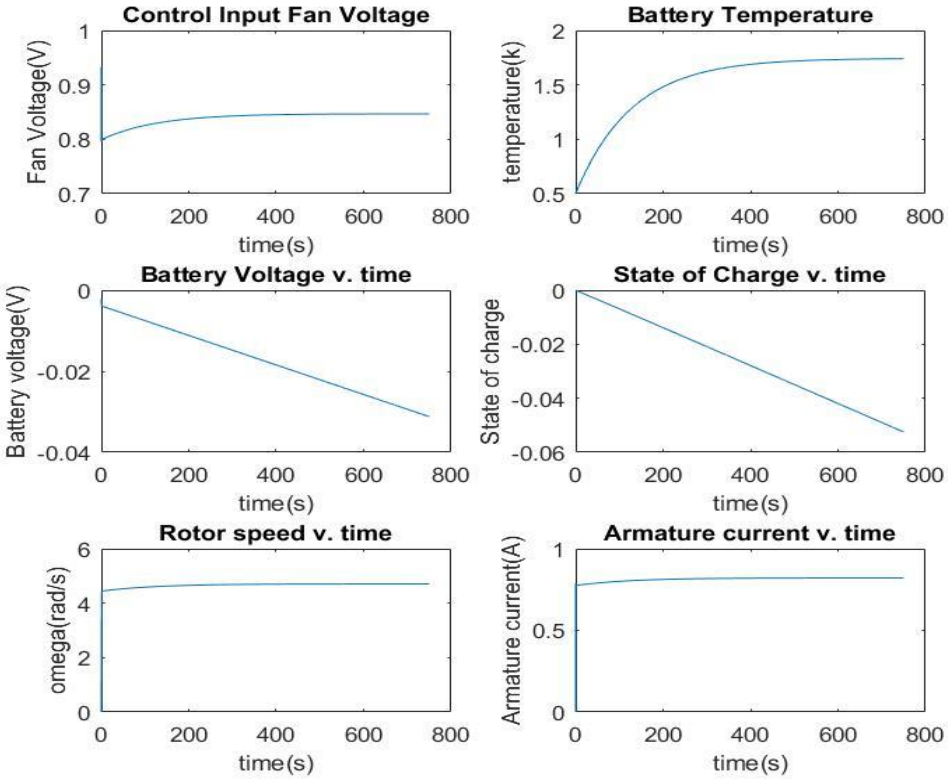

Figure 4.7: LQR w/disturbance responses and disturbance rejection

It is evident based on the results that the disturbance rejection methodology did not work as expected. It did not drive the battery temperature to zero and only provided marginally more temperature reduction than the LQR with no disturbance rejection. In addition, this marginally cooling was provided at the cost of increased control effort and armature current. Based on the results of this simulation, it is evident that the root cause of the controller's inability to drive the temperature variation to zero is that the change in set point due to the current demand increase is not taken into account in this control scheme or the original LQR control scheme. In order to account for the set point change a feedforward controller would have to be implemented along with the LQR. A feedforward controller works by taking into account the impact of a known disturbance (in this case current demand) on the process variable temperature and adding a certain control action to the control input in order to counteract that impact [46]. However, this only works for known disturbances. For unknown disturbances, other forms of robust control will have to be explored. The development of both the feedforward control and the robust control are left to future work.

4.5 SUMMARY

In this chapter the use of a thermal management methodology was proposed for lithium ion batteries. The methodology utilized a fan controlled through optimal control theory to ensure minimal temperature variation within the battery. The system was simulated in SIMULINK and MATLAB and found to be relatively effective in regulating

temperature when exposed to state perturbations. However, this methodology was not effective in regulating temperature when exposed to current demands.

Chapter 5: Conclusion

Battery management systems that conduct accurate estimation of capacity and effective thermal regulation are important to ensuring that Lithium ion batteries have long and productive lives. As the reliability, safety and longevity of lithium ion batteries improves so does the market share they occupy. The increased proliferation of lithium ion batteries in a host of applications is imperative in order to achieve a greener future.

5.1 Summary of Thesis

The work presented in this thesis involved the exploration of methods to estimate capacity for a low-order physics based model of a lithium ion battery. Various methods were implemented and simulated including Joint extended kalman filters, Dual extended kalman filters and Dual unscented kalman filters. It was found through simulation and testing that none of these filters were capable of estimating capacity due to capacity's very weak observability with the measurement (terminal voltage) [13]. These failures prompted a change in strategy that involved the augmentation of the battery model to include solid electrolyte growth interphase physics. An unscented kalman filter was applied to this augmented model and similar issues arose with regard to the observability of the capacity from terminal voltage. After all these failed attempts, a successful methodology was implemented. The methodology was based on work completed by Chao et al where he used the inverse of the coulomb counting equation to back calculate capacity from accurate state of charge estimates from and current measurements [32]. The state of charge estimates were obtained through the use of the original battery model and an extend kalman filter [32]. The SOC was then passed through the inverse coulomb counting equation in order to calculate a capacity at every time step. A certain percentage of this "stream" of capacity values was averaged every hour in order to calculate a

singular value for the capacity during that period. The current sum and average were zeroed out after every hour and saturation limits were imposed on the values coming in from the stream. This methodology was accurate within about 3-4% for capacity values between 90-100% of the initial capacity, but became unacceptably inaccurate at or near the 80% mark.

A thermal management system featuring an optimally controlled fan was applied to the lithium ion battery model. The system was developed using a simple two state fan DC motor model [39], parameters collected by Dr. Victor Yu, and aerodynamic equations based on simple, turbomachinery geometry. The model was implemented in Simulink and underwent a battery of simulations in order to determine both the effectiveness of the fan under open loop control and in order to find an operating point about which to linearize. The fan in open loop mode was found to be effective at limiting the battery's temperature rise in the presence of various current demands. Based on this data an operating point was selected and the Simulink linear analysis tool was used to develop a linear system which could be used for control design. The first controller implemented was a digital linear quadratic regulator that performed adequately when the battery temperature was perturbed with no change in current demand. The response of the controller was too slow for the often rapidly changing nonlinear system; however this result can be seen as a proof of concept. Next, a change in current demand was applied to the system and the results concluded that the controller was incapable of driving the temperature state to zero with the current weighting matrices. However, if the weighting on the input is relaxed the temperature will be driven closer to zero with the cost being an unattainable voltage input. Finally, the LQR controller was augmented with a disturbance rejection scheme that offered little improvement to the temperature response over the pure LQR method. It was determined that the controller could not force the temperature

variation to zero due to the fact that the change in set point caused by the current demand increase was not taken into account.

5.2 FUTURE WORK

5.2.1 Improve performance of capacity estimation

While the methodology proposed in this paper is more accurate than any of the standalone kalman filter methodologies implemented it is still too inaccurate for use in an actual battery management systems. While the error in some test cases is less than 2%, this two percent represents an error of weeks or months relative to the battery life which is restricted from date of first use to when the capacity reaches 80% of its original value. Some possible strategies to improve accuracy would be to add data driven methodologies to correct serious deviations such as neural networks [18]. Another method would be to find a way to dynamically adjust the saturation bounds in order to more accurately represent the variance in the capacity.

5.2.2 Capacity fade prediction

While capacity estimation is useful for diagnostic purposes and accurate state of charge estimation [13], it is also useful for capacity fade forecasting. There have been various methodologies that have been discussed in the literature that could be applied to this work including neural networks [18], particle filters and Monte Carlo methods [16]. The sophistication and accuracy of this low order model combined with the robustness of

the aforementioned methods could make for a fast, robust and accurate prediction scheme.

5.2.3 Robust control schemes for Thermal management system

Linear quadratic regulators are excellent for linear systems but have poor performance when applied to non-linear systems. In order to provide robust control for the entire state space of the lithium ion battery, a new control scheme must be considered. One idea is to implement a gain scheduling scheme were multiple operating points are analyzed similar to the work in this thesis and given gains based on linear quadratic regulator theory. These gains are then put in a schedule that the controller can follow as the battery cycles through the various operating points. Another method that could be applied would be a non-linear controller that could robustly control the temperature throughout the wide and varying states of the battery.

5.2.4 Battery management system implementation and validation

The ultimate goal of this research is for the methodologies developed to be used in an actual battery management system. To this end, the final suggestion for future work is to develop a simple battery management system containing both the thermal management schemes and the capacity estimation and prediction schemes. This system would be tested in simulation then it would be deployed to a microcontroller and the used to monitor and maintain a small lithium ion battery pack. The experiments done with this set up would validate the battery management system.

References

[1] (2016, May), *Transportation Sector Emissions* [Online]. Available: http://www3.epa.gov

[2] *Where We Work/India* [Online].Available: http://www.theicct.org

[3] E. Holodny, (2015, Jun 12), *The 13 fastest-growing economies in the world* [Online]. Available: http://www.businessinsider.com.

[4] Where We Work/China [Online].Available: http://www.theicct.org

[5] Z. Liu, "China's Carbon Emissions Report 2015," Cambridge: Belfer Center for Science and International Affairs, Boston, MA, 2015.

[6] (2016, Jun 13), *Emissions from Hybrid and Plug-in Electric Vehicles* [Online]. Available: http://www.afdc.energy.gov

[7] S. Yayathi, "Control Oriented Electrochemical Modeling of Lithium-ion Battery Cells for Applications in EVs, HEVs and PHEVs," M.S. Thesis, Dept. Mech. Eng., Univ. of Texas, Austin, TX, 2010.

[8] (2016, May), *Bu-204: How do Lithium Batteries Work?* [Online]. Available: http://batteryuniversity.com

[9] J. B. Goodenough, K-S Park, "The Li-ion Rechargeable Battery: A Perspective," *J. of The American Chem. Society*, vol. 135, pp.1167-1176. Jan. 2013.

[10] C. M. Julien, A. Mauger, K. Zaghib, H. Groult, "Comparative Issues of Cathode Materials for Li-ion Batteries," *Inorganics*. vol. 2, pp.132-154. March 2014

[11] (2016, July), *Bu-205: Types of Lithium-ion* [Online]. Available: http://batteryuniversity.com

[12] S. Yang; L. Liu, D. Jin-Ping, Z. Bin, H. Xue-Jie, "Cation mixing (Li0.5Fe0.5)2SO4F cathode material for lithium-ion batteries," *Chinese Physics B*. vol. 20, no. 12, Dec. 2011.

[13] C. Hu, B. D. Youn, J. Chung, "A multiscale framework with extended kalman filter for lithium-ion battery SOC and capacity estimation," *Appl. Energy*, vol. 92, pp. 694-704, April 2012.

[14] A. Barré, B. Deguilhem, S. Grolleau, M. Gérard, F. Saurad, D. Riu,"A Review on lithium-ion battery ageing mechanisms and estimations for automotive applications," *J. of Power Sources*. vol. 241, pp. 680-689, Nov. 2013.

[15] A. Eddahech, O. Briat, N. Bertrand, J-Y. Delétage, J-M. Vinassa, "Behavior and state-of-health monitoring of Li-ion batteries using impedance spectroscopy and recurrent neural networks," *Int. Elect. Power and Energy Systems*. vol. 42, no. 1, pp. 487-494, Nov. 2012.

[16] B. Pattipati, C. Sankavaram, K.R. Pattipati, "System Identification and Estimation Framework for Pivotal Automotive Battery Management System

Characteristics," *IEEE Transactions on System, Man, and Cybernetics*, vol. 41, no. 6, pp. 869-884, Nov. 2011.

[17] W. He, N. Williard, M. Osterman, M. Pecht, "Prognostics of lithium-ion batteries based on Dempster-Shafer theory and the Bayesian Monte Carlo method," *J. of Power Sources*. vol. 196, no. 23, pp. 10314-10321, Dec. 2011.

[18] G. Bai, P. Wang, C. Hu, "A self-cognizant dynamic system approach for prognostics and health management," *J. of Power Sources*. vol. 278, pp. 163-174, Mar. 2015.

[19] N. Buduma, (2015). Data Science 101: Preventing Overfitting in Neural Networks [Online]. Available: http://www.kdnuggets.com

[20] I-S. Kim, "A Technique for Estimating the State of Health of Lithium Batteries Through a Dual-Sliding –Mode Observer." *IEEE Transactions on Power Electronics*. vol. 25, no. 4, pp. 1013-1022, Apr. 2010.

[21] W. Qiuting, J. Yinzhu, L. Yunhao, "State of Health Estimation for Lithium-ion Battery Based on D-UKF," *Int. J. of Hybrid Information Technology*. vol. 8, no. 7, pp. 55-70, Jul. 2015.

[22] R. Sabbah, R. Kizilel, J.R. Selman, S. Al-Hallaj, "Active (air-cooled) vs. passive (phase change material) thermal management of high power lithium-ion packs: Limitation of temperature rise and uniformity of temperature distribution," *J. Power Sources*, vol. 182, no. 2, pp. 630-638, Aug. 2008.

[23] S.A. Khateeb, M.M. Farid, J.R. Selman, S. Al-Hallaj, "Design and simulation of a lithium-ion battery with a phase change material thermal management system for an electric scooter," *J. Power Sources*, vol. 128, no. 2, pp. 292–307, Apr. 2004.

[24] W.Q. Li, Z.G. Qu, Y.L. He, Y.B. Tao, "Experimental study of a passive thermal management system for high-powered lithium ion batteries using porous metal foam saturated with phase change materials," *J. of Power Sources*, vol. 255, pp. 9-15, Jun. 2014.

[25] A. Stupar, U. Drofenik, J.W. Kolar, "Optimization of Phase Change Material Heat Sinks for Low Duty Cycle High Peak Load Power Supplies," *IEEE Transactions on Components, Packaging and Manufacturing Technology*. vol. 2, no. 1, pp. 102-115, Jan. 2012.

[26] C. Alaoui, "Solid-State Thermal Management for Lithium-Ion EV Batteries," *IEEE Transactions on Vehicular Technology*. vol. 62, no. 1, pp. 98-107, Jan. 2013.

[27] L. Fan, J.M. Khodadadi, A.A. Pesaran,"A parametric study on thermal management of an air-cooled lithium-ion battery module for plug-in hybrid electric vehicles," *J. of Power Sources*, vol. 238, pp. 301-312 , Sept. 2013.

[28] S. Mohammadian, Y. Zhang, "Thermal management optimization of an air-cooled Li-ion battery module using pin-fin heat sinks for hybrid electric vehicles," *J. of Power Sources*. vol. 273, pp. 431-439, Jan. 2015.

[29] L.W. Jin, P.S. Lee, X.X. Kong, Y. Fan, S.K. Chou, "Ultra-thin minichannel LCP for EV battery thermal management," *Appl. Energy*, vol. 113, pp. 1786-1794, Jan 2014.

[30] S. K. Mohammadian, Y-L. He, Y. Zhang, "Internal cooling of a lithium-ion battery using electrolyte as coolant through microchannels embedded inside the electrodes," *J. of Power Sources*. vol. 293, pp. 458-466, Oct. 2015.

[31] E. Prada, D. D. Domenico, Y. Cre, J. Bernard, V. Sauvant-Moynot, F. Huet, "A Simplified Electrochemical and Thermal Aging Model of LiFePO4-Graphite Li-ion Batteries: Power and Capacity Fade Simulations." *J. of Elect. Chemical Society*, vol. 160, no. 4, pp. A616-A628, Feb. 2013.

[32] C. Hu, G. Jain, P. Tamirisa, T. Gorka, "Method for estimating capacity and predicting remaining useful life of lithium-ion battery," *Appl. Energy, vol. 126,* pp.182-189, Aug. 2014.

[33] D. Di Domenico, G. Fiengo, and A. Stefanopoulou, "Lithium-Ion battery State of Charge estimation with a Kalman Filter based on a electrochemical model," in 17th IEEE International Conference on Control Applications, CCA, San Antonio, TX, United states, pp. 702-707, 2008.

[34] R. Refai, "Hybrid Neural Net and Physics Based Model of a Lithium Ion battery," M.S. thesis, Dept. Mech. Eng. , University of Texas, Austin, TX, 2011.

[35] G.L. Plett, "Dual and Joint EKF for Simultaneous SOC and SOH Estimation," in *Electric Vehicle Symposium and Exhibition*, Monaco, 2005.

[36] M.R. Mickens, "Discretizations of nonlinear differential equations using explicit nonstandard methods," *J. of Computational and Applied Math.* vol. 110, no. 1, pp. 181-185, Oct. 1999.

[37] Y. Cao (2008) Learning the Extended Kalman Filter (Version 1.0) [Source code]. Available: http://www.mathworks.com/

[38] R. Longoria (1998) Fixed-step RK4 Algorithm [Source code]

[39] E.A. Wan, R. V.D. Merwe, "The Unscented Kalman Filter" in *Kalman Filtering and Neural Networks*. New York: John Wiley & Sons, Inc, 2001, ch.7

[40] M. Bahrami. *Forced Convection Heat Transfer* [Online]. Available: http://www.sfu.ca/

[41] *DC Motor Speed: System Modeling* [Online]. Available: http://ctms.engin.umich.edu/

[42] R.S.R. Gorla, A.A. Khan, "Axial Flow Compressors and Fans," in *Turbomachinery Design and Theory* New York : Marcel Dekker, 2003, ch. 5.

[43] (2011)*Ceiling fan-moment of inertia?* [Forum]. Available: https://answers.yahoo.com/question/index?qid=20111109214219AADCApp [Accessed: July 23, 2016].

[44] H. Peng and G. T.C. Chiu, "Linear Quadratic Optimal Control," *Course Pack of Design and Digital Control Systems, 2012.*

[45] *Tracking and Disturbance Rejection* [Online]. Available: http://www.mathematik.uni-stuttgart.de/

[46] D. Cooper, R. Rice, J. Arbogast, "Tutorial: Cascade vs. Feed Forward for Improved Disturbance Rejection," presented at The Instrumentation, Systems and Automations Society, Houston, TX, 2004.

Vita

Ifedioranma Anyaegbunam was born on February 20th, 1991 in Iowa City, IA. He moved to Lexington, KY in the winter of 2001 where he attended Lafayette High School. In 2009, he received the Singletary Scholarship to attend the University of Kentucky where he graduated summa cum laude with a B.S. in Mechanical Engineering in May 2014. While at the University of Kentucky, he completed internships at General Electric Appliances in Louisville, KY and Toyota Engineering and Manufacturing of America in Erlanger, KY. He went on to attend the University of Texas at Austin in the fall of 2014 to obtain a M.S. degree in Mechanical Engineering where he worked on research involving Lithium ion battery modeling and monitoring.

Perment email: ifedianyaegbunam@gmail.com

This thesis was typed by Ifedi Anyaegbunam